Characterization of Additively Manufactured Mechanical Metamaterials

by

Tark Raj Giri

A thesis submitted to the Graduate Faculty of
Auburn University
in partial fulfillment of the
requirements for the Degree of
Master of Science

Auburn, Alabama
August 07, 2021

Keywords: Metamaterials, auxetic metamaterials, bistable, energy absorption, cylindrical shells

Approved by

Russell W. Mailen, Assistant Professor of Aerospace Engineering
Suhasini Gururaja, Associate Professor of Aerospace Engineering
Kyle Schulze, Assistant Professor of Mechanical Engineering
Eldon Triggs, Lecturer of Aerospace Engineering

Abstract

Designing materials that are lightweight while achieving a desirable combination of mechanical, thermal, and other physical properties is an aspiration in material science. Lattice structures are suitable aspirant to achieve lightweight with precisely tailored mechanical properties because of their porous structures, well-defined geometries of their unit cells, high strength to weight ratio, compared to traditional structural materials. Mechanical metamaterials are engineered structures with unique mechanical properties such as negative Poisson's ratio and bistability which vary dramatically from those of the base material. The unique properties of mechanical metamaterials require accurately fabricated arrangements of ligaments in intricate, periodic structures. AM processes, such as Fused Deposition Modeling (FDM), are able to produce these structures with filaments, such as Thermoplastic Polyurethane (TPU), Polylactic Acid (PLA) which enable precisely fabricated lattice structures. Although recent advancement in AM techniques has enabled the fabrication of various lattice metamaterials with unique properties, still, the cogent designs of mechanical metamaterials with programmable stiffness of auxetic structures and multistability are still difficult and exciting topics. In this regards, we explore the two domains of mechanical lattice metamaterials (i) designing auxetic metamaterials with programmable stiffness and (ii) exploiting planar and cylindrical bistable lattices for mechanical response and energy absorption. These emergent domains indicate the transitioning of mechanical lattice metamaterials from traditional materials to smart, adaptive, and versatile materials, which has applications in realistic problems in energy absorption devices, wearable devices, and robotics, and continue to push the boundary of possibilities of architected metamaterials.

Acknowledgments

I would first like to thank my advisor Russell W. Mailen of the Department of Aerospace Engineering at Auburn University. The help and immense support from Dr. Mailen during my entire research and writing whenever I ran into any trouble spot is highly appreciable. He consistently allowed this paper to be my own work, but steered me in the right direction whenever he thought I needed it. I would also like to thank Dr. Ramsis Farag (Center for Polymers and Advanced Composites at Auburn University) and Garon Griffiths (Auburn University MakerSpace) and Mr. Andy Weldon for their support in preparing and testing samples.

Finally, I must express my very profound gratitude to my parents and other family members for providing me with unfailing support and continuous encouragement throughout my years of study and through the process of researching and writing this thesis. I am really grateful to Rume and my Niece Melissa Nath for bestowing immense positive vibes during my journey. This accomplishment would not have been possible without them. Thank you.

Table of Contents

Abstract ii

Acknowledgments iii

1 Introduction to Lattice Metamaterials 1

1.1 Lattice Structures 1

1.1.1 Additive Manufacturing of lattice structures 2

1.2 Metamaterials and Mechanical Metamaterials 3

1.2.1 Mechanical metamaterials based on Poisson's ratio 4

1.3 Auxetic metamaterials 6

1.3.1 Re-entrant Structures 7

1.4 Multistable Mechanical Metamaterials 8

1.4.1 Curved Bistable Beam 9

1.5 Additive Manufacturing of mechanical metamaterials using fused deposition modeling 13

1.6 Outline of Thesis 15

2 Auxetic Metamaterials 16

2.1 Abstract 16

2.2 Introduction 17

2.3 Design and Experiments 18

2.3.1 Design 18

2.3.2 Properties of PLA 19

2.3.3 Experimental Setup 20
2.4 Experimental results and discussion 20
2.4.1 Bowtie arrays 21
2.4.2 Honeycomb arrays 23
2.5 Conclusion 24

3 Bistable Planar Structure 27
3.1 Abstract 27
3.2 Introduction 28
3.3 Fabrication 28
3.4 Design of repeat unit geometry 29
3.5 Experiment 30
3.6 Results and Discussion 31
3.6.1 Bistable lattices printed in collapsed configuration 31
3.6.2 Bistable lattices printed in expanded configuration 32
3.7 Conclusion 33

4 Multistable Cylindrical Metamaterial 35
4.1 Abstract 35
4.2 Introduction 36
4.3 Materials and Methods 39
4.3.1 Design of Bistable unit cell 39
4.3.2 Relation between F and Q 40
4.3.3 Design of Cylindrical Bistable Structures 42
4.3.4 Fabrication 44
4.3.5 Experiment 45
4.3.6 Finite Element Analysis Methodology 45

4.3.7 Material Model 47
4.4 Results and Discussion 49
4.4.1 Mechanical behavior of Type 1 and Type 2 layers 50
4.4.2 Energy Absorption of Bistable Cylinders 52
4.4.3 Effects of sinusoidal beam thickness on snap-through sequence 55
4.4.4 Finite Element Analysis (FEA) Results 58
4.5 Conclusion 63

5 Summary and Future Work 66
5.1 Summary 66
5.2 Future Work 68

References 72

List of Figures

1.1 Schematic of Fused Deposition Modelling (FDM) showing the polymer in the form of filament that goes into the extruder and comes out from a heated nozzle to print the final product into the build plate. 3

1.2 Traditional or non-auxetic materials are shown on the top, zero Poisson's ratio material in the middle and auxetic/negative Poisson's ratio material is shown in bottom. Traditional materials when subjected to uniaxial tension (compression) contract (expand) in lateral direction. Zero Poisson's ratio material only deform in the direction of applied loading. Auxetic materials when subjected to uniaxial tension (compression) expand (contract) in lateral direction. 5

1.3 Classification of most common auxetic structures with their schematics. Re-entrant structure consists of hexagonal face cells which are protruded inward. A chiral unit consists of a central cylinder that is tangentially enclosed by ligaments. Rotating rigid structures has a rigid square that is connected by simple hinges which acts as a rotating structure. 7

1.4 Schematic of re-entrant structure which shows a unit cell with a positive angle $90° > \alpha > 0°$) and a negative angle $360° > \theta > 180°$) 8

1.5 Curved beam mechanism with the length of l, thickness of t, apex height h. A vertical force F_y is applied at the top and the instantaneous displacement is denoted by d. The beam is constrained at both ends. 9

1.6 The curve shows the viscoelastic behavior of the polymer plotted as Modulus vs temperature. The glass transition temperature (T_g) is where the polymer switches from glassy state to rubbery state. The melt temperature (T_m) is where the polymer starts melting and flows out of the nozzle 14

2.1 Sketch of : (a) bowtie unit cell (b) honeycomb unit cells with the actual dimensions used for 3D printing. Note the orientation of local coordinates in the 2D drawing of the unit cell. 18

2.2 Array of three rows and three columns of bowtie unit cell with space for roller mounting. 19

2.3 Schematic of array with and without defects along with direction of loading. . . 20

2.4 Stress-strain curve for PLA dogbone sample. 21

2.5 Experimental setup: Bowtie array with spot defect oriented for loading in X direction. 22

2.6 Force-displacement curves for bowtie structures loaded in the X-direction: (left) in tension and (right) in compression. 22

2.7 Force-displacement curves for bowtie structures loaded in the Y-direction: (left) in tension and (right) in compression. 23

2.8 Force-displacement curves for honeycomb structures loaded in the X-direction: (left) in tension and (right) in compression. 24

2.9 Force-displacement curves for honeycomb structures loaded in the Y-direction: (left) in tension and (right) in compression. 25

3.1 Stress- Strain curve for dogbone sample of TPU 29

3.2 Collapsed state (a) single repeat unit geometry with all the necessary dimensions used for 3D printing (b) unit cell arranged in an array of three rows and three columns 30

3.3 Bistable repeat unit in expanded state (left) and unit cell arranged in an array of three rows and three columns (right) 30

3.4 Mechanical response of bistable lattices printed and tested in collapsed configuration for the lattices with number of rows and columns varying from 1*1 to 3*3 32

3.5 Mechanical response of different bistable lattices printed in collapsed configuration but tested in expanded state for the lattices with number of rows and columns varying from 1*1 to 3*3 32

3.6 Mechanical response of different bistable lattices printed in expanded configuration and tested in collapsed state for the lattices with number of rows and columns varying from 1*1 to 3*3 33

3.7 Mechanical response of different bistable lattices printed and tested in expanded configuration for the lattices with number of rows and columns varying from 1*1 to 3*3 34

4.1 Mechanical response of a curved beam (a) Curved beam with span l, thickness t, applied force f and its three different states after the application of transverse force f. The structure is stable in State 1 and State 3. The beam takes on an unstable, buckled configuration in State 2. (b) Force-displacement and potential energy-displacement response for a bistable beam in three different states. . . . 40

4.2 (a) Three buckling modes of a curved beam constrained at both ends. Mode 2 and Mode 3 are possible mode shapes during the unstable State 2. (b) Normalized force versus normalized displacement for three different modes. F_2 and F_3 are straight lines with a negative slope that do not depend on Q. Bistability is attained at Q=2.31, shown for reference. 42

4.3 Geometries of basic unit cells for Type 1 (top) and Type 2 (bottom) multistable cylinders. (a) Dimensions of planar unit cells (units in mm). (b) Unit cells projected onto a cylinder with a radius of 74.2 mm and extruded 12.7 mm outward to obtain a cylinder with an outer radius, R = 86.69 mm. (c) Arrays of six unit cells patterned around the cylinder. The orientation of the structure during 3D printing is indicated by the arrow in the upper right-hand corner. 42

4.4 (a) Cylinder comprising six Type 1 layers (1-6) with outer radius R, and height H. (b) Cylinder comprising three Type 2 layers (1-3) with same radius R and height H as in (a). 43

4.5 Test setup showing the testing machine Instron 5565 with a 1 kN load cell, camera setup, specimen, and the customized test fixture. The custom test fixture consists of 12 mm thick aluminum plates with 12 mm diameter aluminum rods for mounting to the tensile tester. 45

4.6 Depiction of finite element models. (a) Single layer Type 1 cylinder with sinusoidal beam thickness of t = 1.5 mm. (b) Six-layer Type 1 cylinder with uniform sinusoidal beam thickness of t = 1.5 mm. (c) Depiction of boundary conditions applied to six-layer cylinder. The bottom is pinned in place and the top displaces axially by a prescribed amount, δ. The meshes in all three images were determined by a mesh convergence analysis. 46

4.7 Mesh convergence analysis for a single Type 1 layer with beam thickness of 1.5 mm. 47

4.8 Mesh convergence analysis based on maximum force to initiate snap-through (left) and energy absorption (right). The results are for a single Type 1 layer with beam thickness of 1.5 mm. 47

4.9 Thermogram from differential scanning calorimetry of TPU filament. There is an apparent Tg at 55.5°C during the second heat. 48

4.10 Dynamic mechanical analysis (DMA) results for a frequency sweep at 26°C. . . 49

4.11 Relaxation modulus calculated from relaxation test in DMA. 49

4.12 Experimental pictures for random snapping sequence when the thickness of sinusoidal beam in all the layers is uniform (1.5 mm). 52

4.13 Force-displacement curves for single layer of (a) Type 1 (green) (b) Type 2 layer (dark red) cylinders. Solid lines show loading (tension) and dashed shows unloading (compression) curves for Type 1 and Type 2 layers. 53

4.14 Comparison of force-displacement curves for Type 1 and Type 2 cylindrical layers with same height and radius. Type 1 consists of six layers and Type 2 consists of three layers. 53

4.15 (a) Schematic representation of area under cyclic loading obtained by Trapezoidal integration. The energy absorbed during loading is represented by the green area, during unloading is represented by the red area, during sequential loading and unloading. (b) Energy absorption during loading (tension) and unloading (compression) for varying number of Type 1 layers. 55

4.16 Energy absorption of individual layers during loading and unloading with thickness of sinusoidal beam ranging from 1 mm to 2 mm at an interval of 0.2 mm. . 56

4.17 (a) Six Type 1 cylindrical layers with varying thickness were assembled in non-sequential order. (b) Snapshots showing the snapping sequence of the multistable cylinder when subjected to cyclic loading. The top row shows the loading (expansion) process in tension with a guided snapping of layers. The bottom row shows the guided collapse of layers in unloading (compression). Red arrows and white text boxes indicate which layer snaps-through in each image. . . 56

4.18 (a) Force - displacement curve for the Type 1 cylinder with layers of varying thickness. The sequence of snapping occurs in order from the least thick beam layer to the thickest. (b) Magnitude of difference between local maximum and minimum forces (ΔF) along the region of negative stiffness region plotted against the number of snap-through. 57

4.19 Computational images for random snapping sequence when the thickness of sinusoidal beam is uniform (1.5 mm). 59

4.20 Computational images for controlled snapping sequence when the thickness of sinusoidal beam varies from 1 mm to 2 mm. 60

4.21 Example from FEA of a deformed Type 1 layer. Contours are for von Mises stress with units in Pa. The inset shows a closeup of the stress contours on the deformed structure. Even though the structure is in its second stable state, the residual stress persists. 60

4.22 FEA results for a single, Type 1 layer with t = 1.5 mm. Computational results (solid lines) are overlaid with experimental results (dashed lines). The green lines are for the loading portion and the red lines are for the unloading portion. . 61

4.23 FEA results for a six-layer, Type 1 cylinder with t = 1.5 mm. Computational results (solid lines) are overlaid with experimental results (dashed lines). The green lines are for the loading portion and the red lines are for the unloading portion. 61

4.24 FEA results for a six-layer, Type 1 cylinder with varying beam thickness. Computational results (solid lines) are overlaid with experimental results (dashed lines). The green lines are for the loading portion and the red lines are for the unloading portion. 62

4.25 Computational results for energy absorption during loading and unloading when (a) varying the number of layers with t = 1.5 mm and (b) individual layers with thickness of sinusoidal beam ranging from 1 mm to 2 mm at an interval of 0.2 mm. 63

5.1 Thermal chamber that could be made with six faces of polycarbonates with a sliding door mechanism in front to insert the sample. Top and bottom faces could be provided with openings to connect the sample with the testing machine 70

5.2 Bistable unit cell in (a) collapsed state (b) expanded state 71

5.3 Eccentric test fixture arrangement of multistable cylindrical structure in (a) collapsed state (b) expanded state 71

Chapter 1

Introduction to Lattice Metamaterials

"When modern man builds large load-bearing structures, he uses dense solids: steel, concrete, glass. When Nature does the same, she generally uses cellular materials: wood, bone, coral. There must be good reasons for it"- M. F. Ashby, University of Cambridge

1.1 Lattice Structures

Natural cellular materials such as wood, cork and bone have been utilised for centuries, and their structure is mimicked in modern technical materials such as manufactured honeycombs and foams. Cellular structures are an attractive option for many design applications, particularly light-weight, due to the high specific strength and stiffness provided by their porous structures. The deformation behaviour of cellular structures also means they are useful for energy absorption applications [1]. Lattice structures are a type of cellular material that has regular repeating structure of their unit cells. Lattices structure can also be defined as two or three-dimensional micro-architectures comprised of a network of nodes and beams, or struts, that substantially reduces the weight and maintain structural integrity. Lattice structures differ from large scale engineered structures such as trusses or frames in terms of their scale – the unit cells of a lattice structure have a millimetre or micrometre scale. Lattice structures can divide large load into smaller stress through multiple-trusses or support structure. Many of the lattice structures are inspired by naturally occurring crystalline structures, for example honeycomb lattice structures are inspired from bee honeycombs.

Following are some of the advantages of using lattice structures:

- High strength-to-weight ratio
- Excellent shock absorption and impact protection
- Desirable vibration and noise dampening

1.1.1 Additive Manufacturing of lattice structures

A number of manufacturing methods such as investment casting, deformation forming, brazing, etc are proposed to manufacture lattice structures. Limitations of such techniques include the fitness of the structures and the actual cell geometry. AM techniques have been developed over the years to produce three dimensional objects from a digital model by the successive addition of materials without the use of specialized tooling. Traditional manufacturing processes are not capable of building complex lattice structure. AM provides an easy way to fabricate complex lattice structures since AM process brings free-form manufacturing possibility. Table 1.1 shows various popular AM techniques along with the range of materials, advantages and disadvantages. SLA used laser to cure liquid resin into hardened plastic to print the parts whereas laser fuses polymer powder to print parts in SLS. Inkjet 3D printing involves the process of deposition of liquid materials or solid suspensions to form a part. Fused Deposition Modeling (FDM) is a widely used AM technique for manufacturing lattice structures. It is chosen from the rest of the techniques because of its wide range of materials choice and also low cost.

Table 1.1: Various FDM techniques with their advantages and disadvantages

Additive Manufacturing	Materials	Advantages	Disadvantages
Steriolithography (SLA)	Polymers: PEG,PCL,PEGDA	Higher resolution	Applicable only to photopolymers and expansive
Fused Deposition Modeling (FDM)	Thermoplastics	More choices of materials and inexpensive	Warping
Selective Laser Sintering (SLS)	Polymers, Ceramics	No post processing required	Slow and expensive
Inkjet	Fibrin, Gelatin	Incorporation of drugs and molecules	Low resolution

The working of Fused Deposition Modelling (FDM) fabrication process is highlighted below:

- Thermoplastic filament from a spool is first loaded into the printer as shown in Figure 1.1. The nozzle is set at the desired temperature. Once the nozzle reaches the targeted temperature, the filament is fed to the extruder head. The melted filament then comes out of the nozzle.

- The extruder head is facilitated with a three axis system that allows it to move in the X, Y and Z directions. The melted filament is extruded in thin strands and is deposited layer by layer in the build plate according to design geometry (supplied as input), where it cools and solidifies. The cooling of the finished part sometimes can be accelerated through the use of cooling fans attached on the extruder head.

- For the final product to be achieved, multiple layers are required. When a layer is finished, the extruder head moves up and a new layer is deposited. This process is repeated until the part is complete.

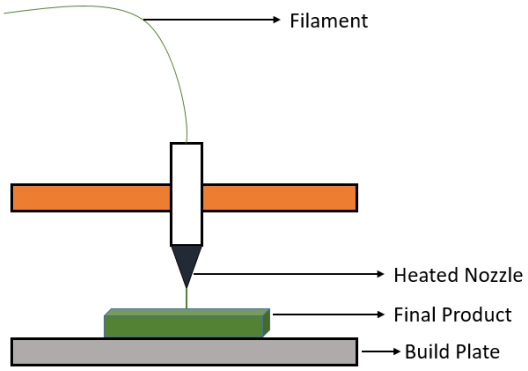

Figure 1.1: Schematic of Fused Deposition Modelling (FDM) showing the polymer in the form of filament that goes into the extruder and comes out from a heated nozzle to print the final product into the build plate.

1.2 Metamaterials and Mechanical Metamaterials

Metamaterials, artificial structures with counter intuitive properties not found in natural materials, have garnered increasing attention during the last few years, the concept of which derived

from the field of electromagnetic materials [2]. Recent advances in design and manufacturing technology, such as AM, have been enabled to fabricate arbitrary complex structures from the microscopic to the macroscopic. In addition, with increasing demands for materials with unusual properties, various metamaterials have evolved, such as electromagnetic metamaterials [3], acoustic metamaterials [4], optical metamaterials [5], thermal metamaterials [6] and mechanical metamaterials [7].

Mechanical metamaterials are engineered lattice structures with properties not found in naturally occurring materials. These materials acquire their unique properties from structure rather than the composition of their internal constituents [8–10]. Structures with regular repeat units possesses desirable properties such as high energy absorption [11–15], vibration isolation [16–18], shock absorption [19, 20], highly sensitive sensors [21–23] and seismic wave protection [24]. Further, the geometry of the unit cell can be designed to obtain unconventional properties such as bistability [25, 26], negative Poisson's ratio (auxetic structures) [27–29], negative compressibility [8, 30] and extremely lightweight with high stiffness [31].

1.2.1 Mechanical metamaterials based on Poisson's ratio

Poisson's ratio is one of the most important parameter to classify mechanical metamaterials. It is defined as the negative ratio of strain along transverse direction to axial direction when uniaxial tensile or compressive load is applied. It is an indicator of what happens in other directions of a material when a load is applied in one direction. Mathematically,

$$\nu = -\frac{\epsilon_{transverse}}{\epsilon_{axial}} \tag{1.1}$$

Generally, mechanical metamaterials can be divided into three main categories based on the Poisson's ratio. Mechanical metamaterials can have Poisson's ratio of positive, zero and, negative.

Typically, mechanical materials having a positive Poisson's ratio, often referred as conventional mechanical materials, i.e., a material expands (contracts) in the direction transverse to the direction of compression (stretching), shown in Figure 1.2. They have found applications

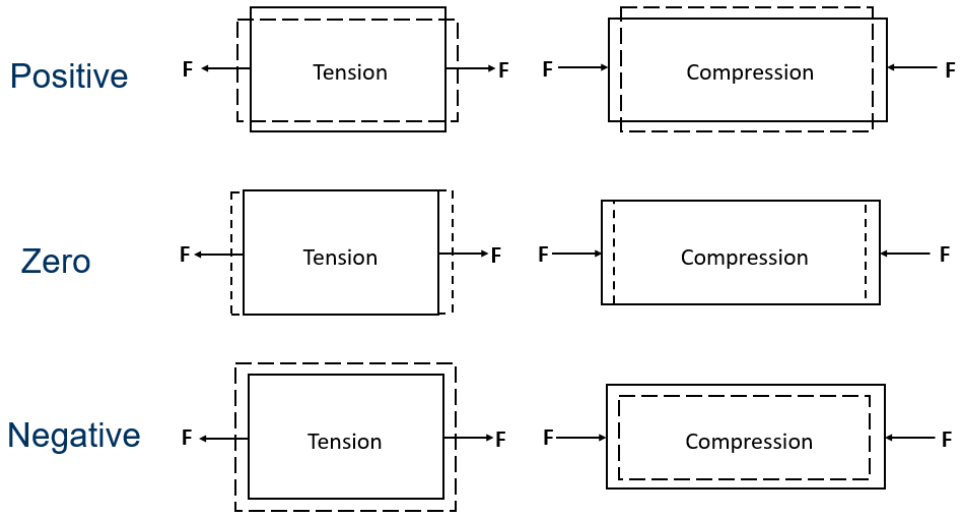

Figure 1.2: Traditional or non-auxetic materials are shown on the top, zero Poisson's ratio material in the middle and auxetic/negative Poisson's ratio material is shown in bottom. Traditional materials when subjected to uniaxial tension (compression) contract (expand) in lateral direction. Zero Poisson's ratio material only deform in the direction of applied loading. Auxetic materials when subjected to uniaxial tension (compression) expand (contract) in lateral direction.

in areas like the design of lightweight structures, development of bio medically relevant materials and rational design of actuators for soft robotic applications. In many of these application areas, lattice structures with positive Poisson's ratio are not only important in their own right but also in combination of other metamaterials.

Mechanical metamaterials with a negative Poisson's ratio are called as auxetic metamaterials because they expand perpendicular to an applied tension instead of shrinking, shown in Figure 1.2 (bottom). Numerous studies have been carried out in auxetic metamaterials in recent years [32–36]. Some of the polymeric structures that achieve negative Poisson's ratio are re-entrant honeycomb structures [37–39], chiral structures [40–42], and rotating element structures [43], which are shown in Figure 1.3. Negative Poisson's structures have numerous advantage over conventional structures such as improved energy absorption [44], shear resistance [45], indentation resistance [46] and fracture resistance [47]. Therefore, negative Poisson's ratio structures are extensively used in textile materials [48], protective tools [49], biomedicine [50], and various other fields.

Mechanical metamaterials with zero Poisson's ratio have constant lateral dimensions under an axial loading (tension or compression). They have applications in areas where shape

change or deformation is required only in one direction without any change in shape or deformation in the direction perpendicular to the applied force [51]. Cork is a good example to understand zero Poisson's ratio material that has a zero Poisson's ratio. Cork can be used as a stopper in blood bottle, since blood bottle are always in tensile load when it is in use (i.e upside down condition). Since cork has zero Poisson's ratio, leakage of blood does not occur as lateral contraction is zero. Lattice structures such as bistable structures are designed that has zero Poisson's ratio which are discussed in Chapter 3 and Chapter 4.

In this thesis, two important mechanical metamaterials are presented namely auxetic structures which has negative Poisson's ratio and bistable structures which has zero Poisson's ratio.

1.3 Auxetic metamaterials

In 1991, Evans [52] first introduced the term of "auxetics", deriving from the Greek word - "auxetikos" which means "that which tends to increase", into the study of materials with negative Poisson's ratio. Afterwards, man-made negative Poisson's ratio structures have attracted increasing attention due to their interesting mechanical properties (e.g. negative Poisson's ratio), as well as emergence of advanced manufacturing technology (e.g. 3D printing). As discussed earlier, negative Poisson's ratio structures expand laterally when pulled longitudinally. Owing to this unusual characteristic behavior, the materials with negative Poisson's ratio have several advantages such as high shear modulus, high damping resistance, high fracture toughness, enhanced crack growth resistance and high energy absorption capability. With these enhanced properties, these structures have enormous potential in the fields of medicine, aerospace, sensors and actuators, etc.

With comprehensive investigation of auxetic deformation mechanism, some well established auxetic structures are proposed and identified, such as chiral structures [53], re-entrant structures [54] and rotating rigid structures [55], refer Figure 1.3. Auxetic behavior is usually obtained through special structural design, i.e., consisting of periodically arranged auxetic units. Re-entrant structure consists of hexagonal face cells which are protruded inward. A chiral unit consists of a central cylinder that is tangentially enclosed by ligaments. Rotating rigid structures has a rigid square that is connected by simple hinges which acts as a rotating

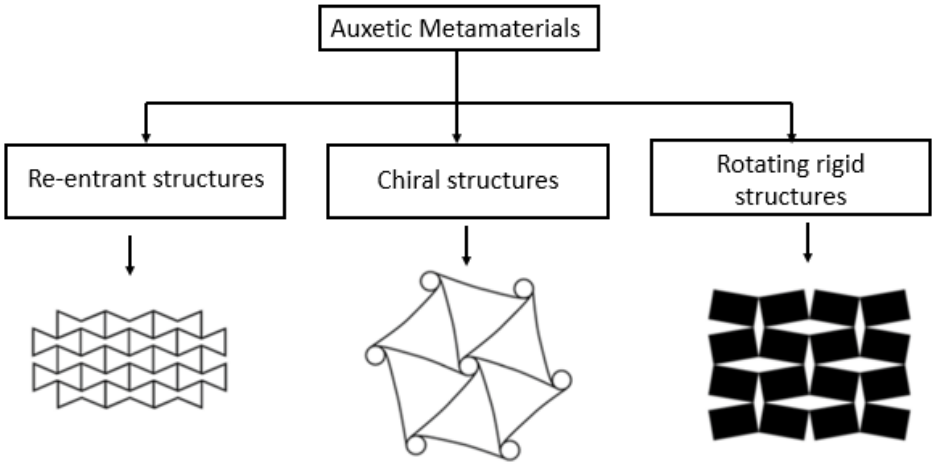

Figure 1.3: Classification of most common auxetic structures with their schematics. Re-entrant structure consists of hexagonal face cells which are protruded inward. A chiral unit consists of a central cylinder that is tangentially enclosed by ligaments. Rotating rigid structures has a rigid square that is connected by simple hinges which acts as a rotating structure.

structure. As one of the major focus of this thesis is to study re-entrant structures, upcoming section gives highlights on re-entrant structures.

1.3.1 Re-entrant Structures

The mechanical properties of the lattice structures can be changed by varying the connectivity of the struts and the angles between the struts at joints, therefore creating auxeticity. Re-entrant structure is a typical auxetic structure, which consists of periodic arrangements of hexagonal units having two negative angles ($360^\circ \geq \theta > 180^\circ$), as shown in Figure 1.4. Any interior angle in a polygon which is more than 180° is known to be a negative angle. The auxetic behavior in re-entrant structure is attributed to the bending of diagonal ligaments along with the outward displacement of vertical ligaments when it is uniaxially stretched horizontally. [56].

Re-entrant structure was first proposed in 1980s and it has gained significant importance because of its simple structure and auxeticity [57]. Design, analysis and optimization of re-entrant structures have been a crucial research area in the recent years. Rotation, bending and, buckling are three major mechanisms of deformation in a re-entrant structure that influences the mechanical properties [58]. Alderson et al [59] studied the behaviour of re-entrant structures under out of plane bending and showed that they undergo dome shape curvature deformation.

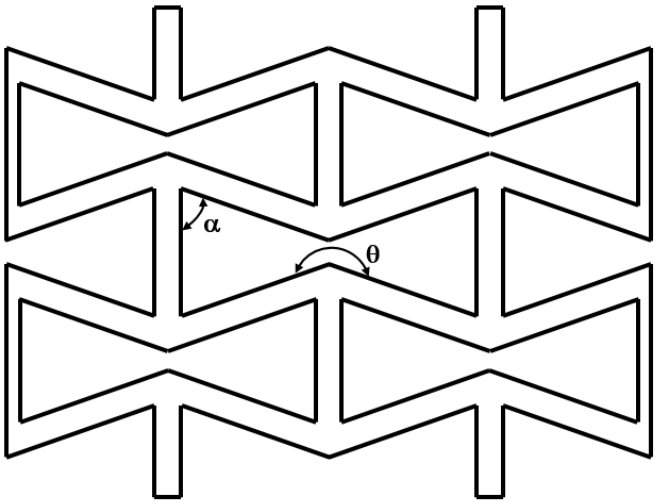

Figure 1.4: Schematic of re-entrant structure which shows a unit cell with a positive angle $90° > \alpha > 0°$) and a negative angle $360° > \theta > 180°$)

Initial cell angle and cell wall thickness effects on the auxeticity was investigated by Zhang et al [60]. Researchers have proposed novel negative Poisson's ratio honeycomb consisting of a re-entrant hexagonal component [61]. The cell size ratio and the re-entrant angle were varied to tune the effective stiffness, negative Poisson's ratio and the rate of cell opening. Researches have been carried out to investigate the static and dynamic mechanical properties for dynamic crushing and indentation on re-entrant structures [62].

1.4 Multistable Mechanical Metamaterials

Multistable mechanical metamaterials are a class of metamaterials which have two or more stable configuration. The multiple stable configurations are reversible in nature which can be utilized to achieve recoverable energy absorption unlike the permanent losses that occur due to damage, plasticity, friction, or viscosity. Switching from one stable configuration to another stable configuration is achieved by overcoming the energy barrier that bridges two stable configurations. Multistable structure consists of arrangements of multiple bistable unit cells in the shape of curved beam. These materials are extensively researched due to their considerable potential for energy trapping [63] or wave guiding [64]. Such structures are 2D patterns extruded into 3D space, therefore, Fused Deposition Modeling is often employed. Moreover, the amount of energy absorption is dependent on small changes in the geometry or

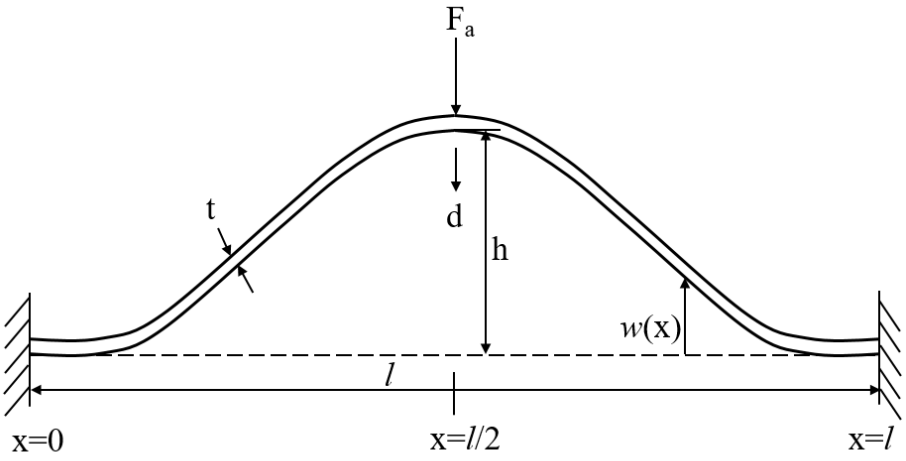

Figure 1.5: Curved beam mechanism with the length of l, thickness of t, apex height h. A vertical force F_y is applied at the top and the instantaneous displacement is denoted by d. The beam is constrained at both ends.

the modulus, which can both be easily achieved using Fused Deposition Modeling. Scholars have demonstrated that these 2D snapping structures could be extended into three dimensions for increased energy absorption and versatility using Fused Deposition Modeling [64, 65]. The ability to construct these structures in 3D configurations is an important step to employing these designs in more applications.

1.4.1 Curved Bistable Beam

For design and analysis of the multistable structures, it is important to understand the mechanism of a bistable unit cell. The bistable unit cell is derived from the curved beam as shown in Figure 1.5. Following section describes the analytical model of a curved bistable beam mechanism [25]:

The governing beam equation for axially compressed straight beam subjected to the boundary conditions shown in Figure 1.5 is:

$$EI\frac{d^4w}{dx^4} + F_a\frac{d^2w}{dx^2} = 0 \tag{1.2}$$

where w is the lateral beam deflection, E is the Young's Modulus of the material of the beam, I is the moment of inertia of the beam and F_a is the axial compressive force.

For a beam clamped at both ends as shown in Figure 1.5, the boundary conditions are:

$$w(0) = w(l) = 0 \tag{1.3}$$

And,

$$\left(\frac{dw}{dx}\right)_{x=0} = \left(\frac{dw}{dx}\right)_{x=l} = 0 \tag{1.4}$$

Normalizing the axial force by:

$$N^2 = \frac{F_a l^2}{EI} \tag{1.5}$$

Non-zero solutions can be obtained, if N satisfies the following criteria:

$$sin\left(\frac{N}{2}\right)\left[tan\left(\frac{N}{2}\right) - \frac{N}{2}\right] = 0 \tag{1.6}$$

With this, equation 1.2 yields following solultions:

$$w(x) = \sum_{i=1}^{\infty} B_i w_i(x) \tag{1.7}$$

where,

$$w_i(x) = B_i\left[1 - cos\left(N_i\frac{x}{l}\right)\right] \tag{1.8}$$

and

$$N_i = (i+1)\pi \tag{1.9}$$

at $i = 1, 3, 5, ...$ And,

$$w_i(x) = B_i\left[1 - 2\frac{x}{l} - cos\left(N_i\frac{x}{l}\right) + \frac{2sin\left(N_i\frac{x}{l}\right)}{N_i}\right] \tag{1.10}$$

and,

$$N_i = 2.86\pi, 4.92\pi, ... \tag{1.11}$$

at $i = 2, 4, 6, ...$ Different buckling modes can be obtained from the above solutions as the beam switches form one stable state to another stable state. $w_i(x)$ being the mode shape and B_i being

the amplitude at different modes. The equation defining the beam shape is:

$$w_0(x) = \frac{h}{2}\left(1 - cos\left(2\pi\frac{x}{l}\right)\right) \tag{1.12}$$

where h is the initial apex height of the beam.

From Hooke's law, the axial compressive force as a result of shortening of the beam's total length after the application of vertical force f_y is:

$$F_x = -E * a * dl \tag{1.13}$$

where $a = bt$ is the cross-sectional area and dl is the change in beam length.

The lateral deflection of the beam at the mid-point $\left(x = \frac{l}{2}\right)$ is given by:

$$d = w_0\left(\frac{l}{2}\right) - w\left(\frac{l}{2}\right) \tag{1.14}$$

The total length of the curved beam with small deflection assumption can be written as:

$$l_{total} = \int_0^l \left(1 + \left(\frac{dw}{dx}\right)^2 dx\right)^{\frac{1}{2}} \tag{1.15}$$

$$l_{total} \approx \int_0^l 1 + \frac{1}{2}\left(\frac{dw}{dx}\right)^2 dx \tag{1.16}$$

If U_b, U_c and U_a are the variations in bending energy, compression energy and acivation energy during deflection, the overall potential energy variation is given by:

$$U_{overall} = U_b + U_c + U_a \tag{1.17}$$

where,

$$U_b = \int_0^l \frac{EL}{2}\left(\frac{d^2w_0}{dx^2} - \frac{d^2w}{dx^2}\right)^2 dx \tag{1.18}$$

$$U_c = -F_x(\Delta l) \tag{1.19}$$

$$U_a = -F_y(\Delta d) \tag{1.20}$$

Using normalization's from [25]:

$$X = \frac{x}{l}, \qquad W(x) = \frac{w(Xl)}{h}, \qquad F = \frac{F_y l^3}{EIh} \tag{1.21}$$

$$\Delta = \frac{d}{h}, \qquad L = \frac{l_{total} l}{h^2}, \qquad A_i = \frac{B_i}{h}, \qquad Q = \frac{h}{t} \tag{1.22}$$

$$U_B = \frac{U_b l^3}{EIh^2}, \qquad U_C = \frac{U_c l^3}{EIh^3}, \qquad U_A = \frac{U_a l^3}{EIh^2} \tag{1.23}$$

Using equations, results in the following normalized equations:

$$\Delta = 1 - 2 \sum_{i=1,5,9,\ldots} A_i \tag{1.24}$$

$$L = 1 + \sum_{i=1}^{\infty} \frac{A_i N_i^2}{4} \tag{1.25}$$

$$\frac{N^2}{12Q^2} = \frac{N_1^2}{16} - \sum_{i=1}^{\infty} \frac{A_i^2 N_i^2}{4} \tag{1.26}$$

The normalized overall potential energy variation can be expressed as:

$$U_{overall} = \left(\frac{N_1^4 - N^2 N_1^2}{2} A_1 - \frac{N_1^4}{4} + 2F \right) A_1 + \left(\frac{N_2^2 - N^2 N_2^2}{4} \right) A_2^2 + \left(\frac{N_3 - N^2 N_3^2}{4} \right) A_3^2 + \sum_{i=4,6,\ldots} \left(\frac{N_i^4 -}{} \right.$$

The analysis of the first three modes with second mode constrained yields normalized forces for first and third mode as:

$$F_1 = \frac{3\pi^4 Q^2}{2} \Delta \left(\Delta - \frac{3}{2} + \sqrt{\frac{1}{4} - \frac{4}{3Q^2}} \right) \left(\Delta - \frac{3}{2} - \sqrt{\frac{1}{4} - \frac{4}{3Q^2}} \right) \tag{1.27}$$

$$F_2 = \frac{N_1^2 (N_3^2 - N_1^2)}{8} \left(\frac{N_3^2}{N_3^2 - N_1^2} - \Delta \right) \tag{1.28}$$

$$F_3 = 8\pi^4 - 6\pi^4 \Delta \tag{1.29}$$

Above equations shows the relationship between the normalized compressive force and displacement of a unit cell. These equations relates the force and displacement based on the mode of deformation of the curved beam which is further discussed in Chapter 4. F_1 depends on Q whereas F_2 and F_3 are straight lines which are not dependent on Q. The bistability is achieved when the value of $Q \geq 2.31$ [25]. Further analysis of these equations on bistability is discussed in Chapter 4 in detail.

1.5 Additive Manufacturing of mechanical metamaterials using fused deposition modeling

The fabrication of mechanical metamaterials using additive manufacturing provides multiple benefits over traditional machining. Using traditional machining to manufacture a mechanical metamaterial structures with complex geometries is very difficult. With additive manufacturing techniques, even the complex metamaterial structures can be fabricated with a great surface finish making rapid prototyping more cost-effective and efficient. Advances in Fused Deposition Modeling (FDM) printers has enabled the fabrication of flexible planar and cylindrical and metamaterials structures effectively which has wide applications in energy absorption and reconfigurale structures [64].

Viscoelasticity and glass transition temperature are two important parameters to be considered during the fabrication of various simple and complex geometric metamaterials using polymeric materials. Polymers are usually described as viscoelastic materials, a general term emphasizes their intermediate position between viscous liquids and elastic solids. If the polymers are heated, there is a temperature at which they change from being a stiff, brittle, and a glass-like material to a rubbery material, refer Figure 1.6. This temperature is called the glass transition temperature (T_g). If the glass transition temperature of the polymeric filament used to fabricate metamaterials lies near the room temperature range, viscoelastic effect needs to be taken into consideration during the mechanical test and simulation of those structures. This also effects the printing parameters such as nozzle temperature, print velocity and, the build plate temperature which, overall, effects the print quality.

The polymeric filaments used for 3D printing of the mechanical metamaterials in this thesis are Polylactic Acid (PLA) and Thermoplastic Polyurethane (TPU). PLA is in glassy

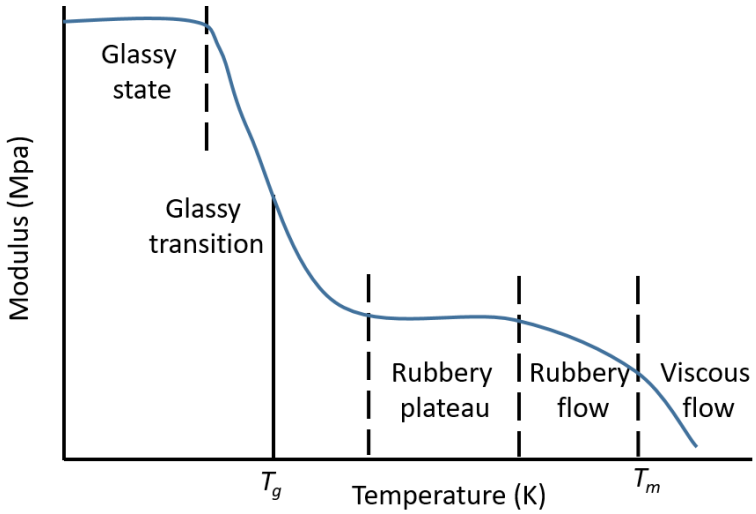

Figure 1.6: The curve shows the viscoelastic behavior of the polymer plotted as Modulus vs temperature. The glass transition temperature (T_g) is where the polymer switches from glassy state to rubbery state. The melt temperature (T_m) is where the polymer starts melting and flows out of the nozzle

state at room temperature whereas TPU is in rubbery state. It is because the glass transition temperature (T_g) of PLA is approximately $65°$C whereas for TPU is around $-45°$C. TPU is in flexible state at room temperature. With flexible filament, it's difficult to print because when it travels from the inlet of the extruder to the nozzle, there is a good chance of warp inside the extruding gears. On the other hand, PLA is easy to print with as it is rigid with limited flexibility at the time of feed to the extruder. 3D printing using Fused Deposition Modeling (FDM) requires the polymer to melt before the actual part is manufactured. The melt temperature (T_m) of PLA and TPU are $175°$C and $145°$C respectively. It is at this temperature where the polymer starts to flow viscously, refer Figure 1.6. So, the polymer used for 3D printing should have sufficient viscosity to ensure that the polymer after melting from the nozzle has desirable velocity. It is always suggested that the nozzle temperature be set higher than T_m so that the polymer has sufficient viscosity to ensure that the polymer after melting has a desirable velocity. Typically, for PLA and TPU, the nozzle temperature is set at a range of $200 - 215°$C and $220 - 235°$C respectively. PLA prints well with the default settings of the printer, however, TPU can be difficult to print with because of the warping issue. Appropriate supports can be generated using software such as MeshMixer for printing with TPU. This highly reduces the warping issue. Another factor to consider is the instant adhesion of deposited layers of melted

polymer. It should also be provided with enough cooling process to ensure final mechanical properties. With the supports generated using MeshMixer, the print speed of 85%, nozzle temperature of 220°C and, bed temperature of 50°C seems to work pretty good for TPU.

1.6 Outline of Thesis

This thesis is divided into five chapters. Chapter 1 has explained the background of metamaterials as well as the recent development of mechanical metamaterials. This chapter further provided information on practical use cases of these structures in the field. Chapter 2 discusses on auxetic metamaterials. This chapter focuses on design, fabrication and testing of various combination of auxetic structures to tune their stiffness. Chapter 3 discusses about the bistable planar structures. This chapter includes design and fabrication of additively manufactured bistable planar structures which are tessellated to form a multistable structure. Finally, this chapter discusses the mechanical behaviour of these structures. Chapter 4 discusses recent developments in the field of multistable structures. This chapter progresses from the bistable planar structure in Chapter 3 to bistable cylindrical structure. This chapter discusses the mechanical behavior of those structures with the changing design parameters. This chapter also discusses the methods of tuning the energy absorption features of multistable cylindrical structures. Chapter 5 concludes with the summary of the thesis and future works to be done.

Chapter 2

Auxetic Metamaterials

This chapter originally appeared in the proceedings for the 2020 SPIE Conference on Smart Structures and Non-Destructive Evaluation (SS:NDE) [27].

2.1 Abstract

In mechanical metamaterials, geometry and material properties dictate the structural response to mechanical loads. These materials are comprised of a tessellated array of repeat unit cells, which form a lattice that populates the domain of the structure. While the mechanical behavior of 2D lattices is well understood, recent advances in polymer based Additive Manufacturing (AM) usher in a new era of metamaterials research. However, previous work in this area has failed to address the effects tessellation of mismatched repeat unit cells of polymer-based mechanical metamaterials. We seek to investigate the effects of combination of bowtie and honeycomb unit cells on the mechanical properties of mechanical metamaterials, in particular, the stiffness. Towards this goal, in the present chapter, an experimental approach is used to investigate the mechanical behaviour of 2D lattice structures. Experimental samples are prepared using Fused Deposition Modeling (FDM) AM. These samples are subject to quasi-static mechanical tests at room temperature. We investigate the effects of mismatched unit cells (defects) on the mechanical behavior of the lattice. Mechanical metamaterials with adjustable stiffness properties have applications in the aerospace and automotive industries, including sandwich composites, damping and impact protection.

2.2 Introduction

Generally, when a material is subjected to a tensile force in the longitudinal direction, the transverse direction contracts and vice-versa, i.e., the material possesses a positive Poisson's ratio [66]. Contrary to this are auxetic materials which exhibit negative Poisson's ratio, that is, they expand in transverse direction when subjected to tension in the longitudinal direction and vice versa [67]. Recently, auxetic materials have gained significant attention because of their better indentation resistance [68], improved fracture toughness [69], high volume shrinkage [70], negative swelling behaviour [71], negative thermal expansion [6], graded stiffness [72] and remarkable energy absorption properties [73]. Auxetic metamaterials with regular repeat units are difficult to fabricate using traditional manufacturing techniques [74], so there is need to make use of AM techniques to fabricate these structures.

Researchers have investigated the mechanical properties of auxetic materials comprised of re-entrant honeycomb (bowtie) shapes under tension and compression [75–77]. Most research efforts have focused on the mechanical properties of metallic lattice structures. An analysis of the effects of geometric design parameters on the mechanical properties of metallic bowtie and honeycomb structures has been carried out [78, 79]. Further, these studies have been performed under quasi-static loading conditions. For instance, Zhang et al. [75] fabricated re-entrant honeycomb structure using stainless steel and loaded the structures at a rate of 3 mm/min. However, there are limited studies on polymeric auxetic metamaterials AM [80–84]. Rafsanjani et al. [85] fabricated structures made up of rubber possessing both auxeticity and bistability and assessed their performance through mechanical testing. Other examples include the mechanical behaviour of Nylon 12 [86], PLA [87, 88], and TPU [89] lattices fabricated by FDM. These studies have focused primarily on honeycomb structures. Thus, limited experimental investigations of auxetic polymer lattices have been performed with no attempt to combine bowtie and honeycomb repeat units to study their mechanical behaviours.

This chapter focuses on performing quasi-static tensile and compression tests on re-entrant honeycomb (bowtie) and honeycomb structures fabricated using FDM 3D printing of PLA filament. Additionally, we will discuss the possibility of tuning stiffness of the fabricated samples

with the introduction of various kinds of defects in the form of mismatched repeat units. The compliance of the systems in tension and compression will then be compared.

2.3 Design and Experiments

This section discusses the basic design and geometric parameters of the repeat unit cells (Section 2.3.1). It also reports the properties of parent material, PLA, in Section 2.3.2. It is followed by Section 2.3.3 on experimental setup and test fixture.

2.3.1 Design

The bowtie and honeycomb structures were designed using SOLIDWORKS. Views of the individual unit cells with their final dimensions are shown in Figure 2.1. All the dimensions are in millimeters (mm). The out-of-plane thickness out of the structures is 8 mm. The structures were printed with PLA using a Makerbot Replicator+ 3D printer. The overall dimensions of the samples were limited by the build volume of the 3D printer, which was 295 L X 195 W X 165 H mm.

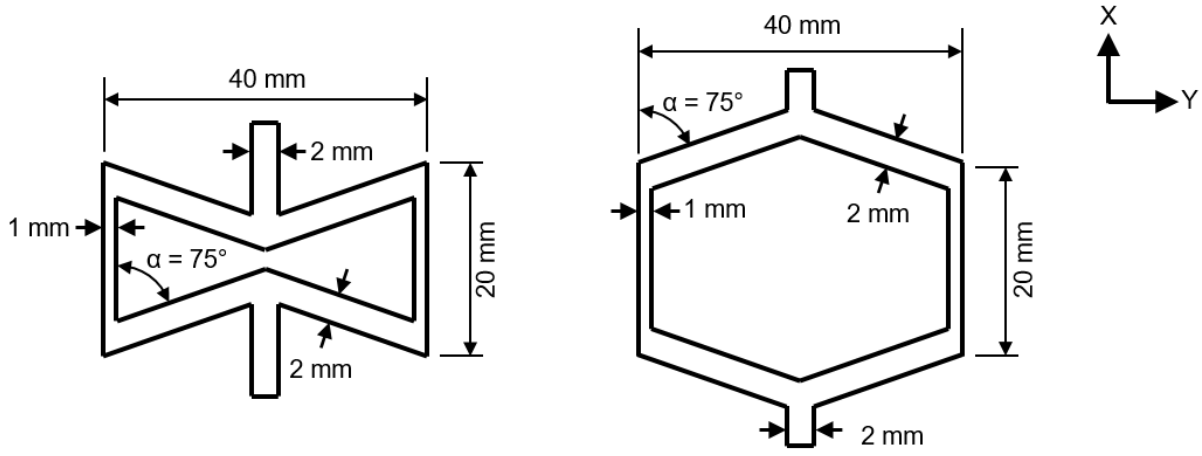

Figure 2.1: Sketch of : (a) bowtie unit cell (b) honeycomb unit cells with the actual dimensions used for 3D printing. Note the orientation of local coordinates in the 2D drawing of the unit cell.

Individual unit cells were arranged in an array of m=3 rows by n=3 columns adjacent to each other as shown in Figure 2.2. This led to the naming convention of a 3*3 array. In total, eight 3*3 arrays were designed. Four arrays were composed primarily of bowtie repeat units, and the rest were composed of primarily honeycomb repeat units. Within each of these sets, three of the arrays contained defects, or mismatched repeat units. The mismatched repeat units occupied either the central repeat unit cell location (cell (2,2), referred to as the spot defect), the central row (m = 2, referred to as the row defect), or the central column (n=2, referred to as the column defect). A schematic representation of defects is shown in Figure 2.3. The overall dimension for 3*3 bowtie and honeycomb were 35.40*61 and 53.06*61 respectively.

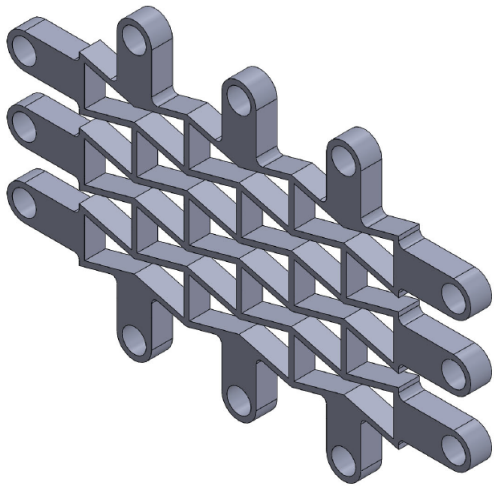

Figure 2.2: Array of three rows and three columns of bowtie unit cell with space for roller mounting.

2.3.2 Properties of PLA

PLA has a glass transition temperature of approximately 45-60°C and a modulus of 0.35-3.5GPa at room temperature 25°C [90]. In order to have a general idea of the mechanical property of the fabricating polymer (PLA), a dog bone sample of PLA (shown in Figure 2.4) was 3D printed in Makerbot Replicator+ at a temperature of 215°C and infill density of 90%. The value for Young's modulus of elasticity was found to be 1.3 GPa using ASTM D638-14.

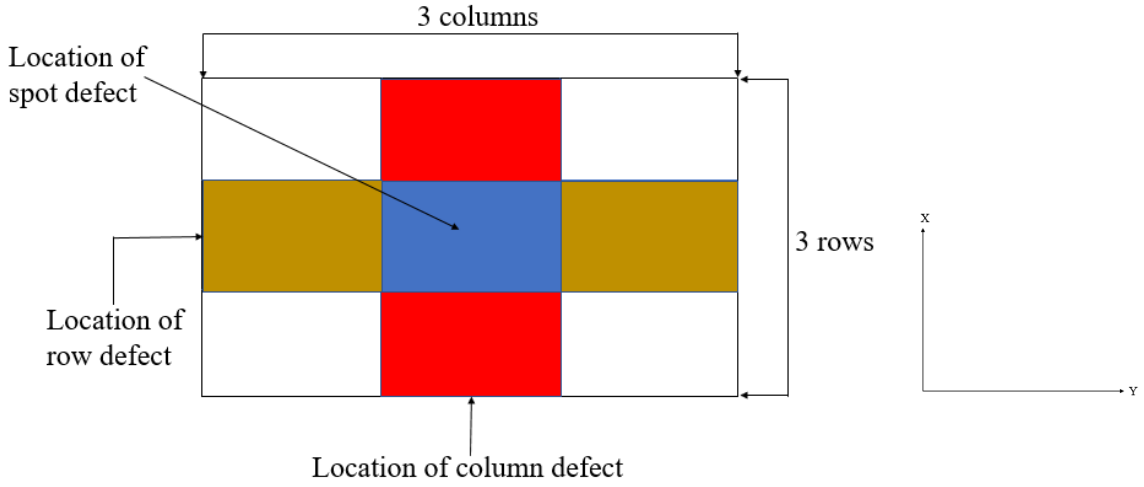

Figure 2.3: Schematic of array with and without defects along with direction of loading.

2.3.3 Experimental Setup

The specimens were subjected to uniaxial tensile and compression test at room temperature (25°C) to measure the mechanical behaviour of the printed structures. A universal testing machine, Instron 5565 with a 5 kN load cell, was used for the experiment under displacement controlled loading. A custom test fixture was designed as shown in Figure 2.5. The edges of the structure were modified with thick struts that could fit a circular strut going through the hole. Rollers were incorporated on each circular strut, except on the central repeat unit. This allowed to hold the sample while allowing for transverse expansion and contraction. Each sample was tested in two principal directions, X and Y as shown in Figure 2.3, by rotating the sample in the test fixture. The unit cell was modified at the sample boundaries to incorporate tabs for mounting the sample. Rollers were used along the tabs to allow lateral displacement of the sample. The test was conducted at at strain controlled rate of 4 mm/min, and the test was stopped when the strain was approximately 10%.

2.4 Experimental results and discussion

Each of the printed 3*3 arrays were subjected to tensile and compression tests using the setup shown in Figure 2.5. The results are presented as force-displacement curves due to the similar

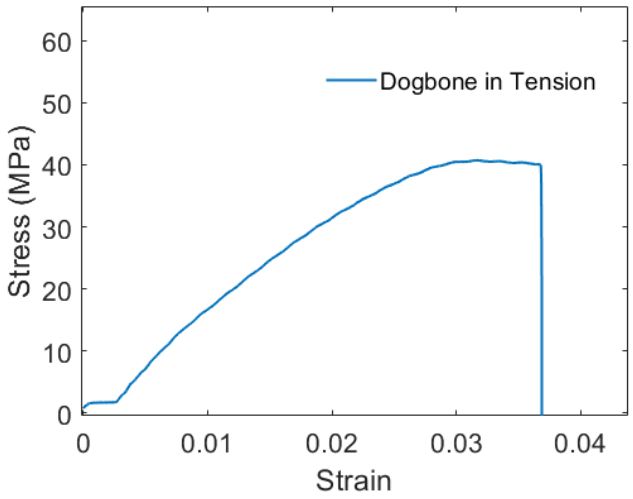

Figure 2.4: Stress-strain curve for PLA dogbone sample.

external dimensions of the compared structures within a set and the porous nature of the lattice. As expected, bowtie samples loaded in tension in the X-direction expanded in Y-direction. When these samples were loaded in compression in the X-direction, they contracted in the Y-direction. Similar behavior was seen for tension and compression loading in the Y-direction. This indicates the negative Poisson's ratio for both testing directions. As expected, the honeycomb arrays displayed a positive Poisson's ratio, contracting in the transverse direction when loaded in tension, and expanding in the transverse direction when loaded in compression.

In general, relatively linear force-displacement curves were obtained for all structures tested in X-direction as shown in Figures 2.6, 2.8, and non-linear curves were obtained when loaded in Y-direction as shown in Figure 2.7 and, Figure 2.9. Comparing the results obtained for tensile loading in Y direction shows similar trends as reported by Zhang et al. [75].

2.4.1 Bowtie arrays

2.4.1.1 Bowtie arrays with and without defects loaded in X-direction

The first set of experiments evaluated the stiffness of lattices containing primarily bowtie unit cells. Results for samples tested in the X-direction are shown in Figure 2.6. The curve for pure bowtie array in Figure 2.6, left, is low compared to the other curves in this set. During the experiment, it was observed that the rollers did not exactly rest on the surface of test fixture

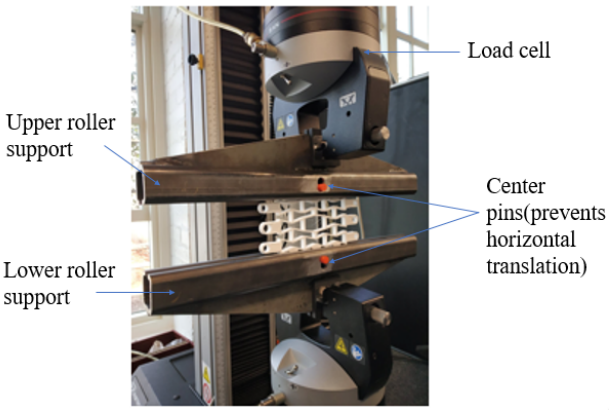

Figure 2.5: Experimental setup: Bowtie array with spot defect oriented for loading in X direction.

due to a loading error. Thus, the array was not able to take load during testing. However, the results are included here for the completeness of the data-set. In Figure 2.6, it is seen that the position of the defects within the primarily bowtie lattice varied the stiffness of the structure. It is observed in Figure 2.6, left, that the honeycomb row array (i.e. a bowtie array with a row of honeycomb unit cells) loaded in tension, has the highest stiffness. However, in compression, the honeycomb column array shows the highest stiffness, as shown in Figure 2.6, right.

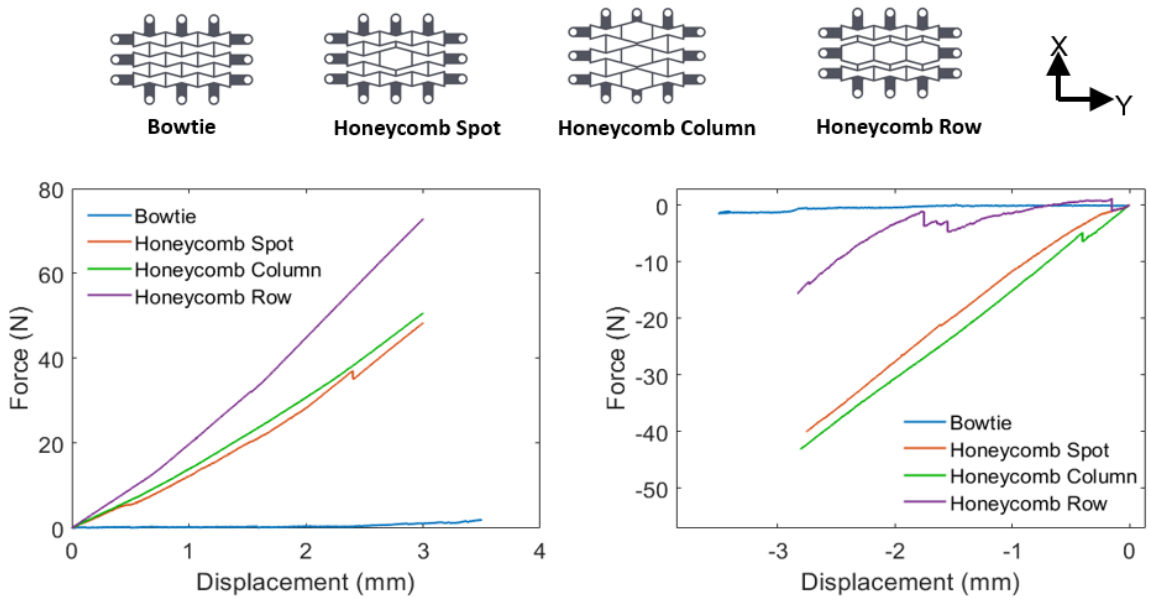

Figure 2.6: Force-displacement curves for bowtie structures loaded in the X-direction: (left) in tension and (right) in compression.

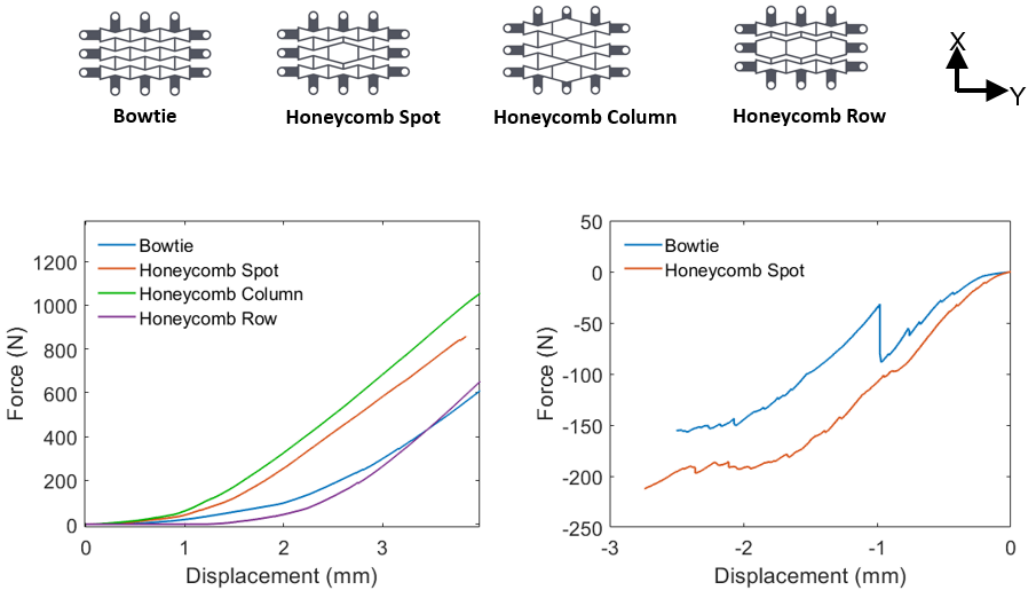

Figure 2.7: Force-displacement curves for bowtie structures loaded in the Y-direction: (left) in tension and (right) in compression.

2.4.1.2 Bowtie arrays with and without defects loaded in Y-direction

Results for tension tests of the bowtie lattices conducted in the Y-direction, Figure 2.7, left, indicate that the array with a column of honeycomb repeat units is less complaint. Incorporating a row defect results in an initial decrease of the stiffness compared to the regular 3*3 bowtie structure. Compression tests in the Y-direction for the bowtie structures could only be performed for two structures because the other two samples failed during the unloading from tension. The two arrays tested in compression are the bowtie array and the bowtie array with a single honeycomb repeat unit in the middle (honeycomb spot). The latter of these two arrays was stiffer, as shown in Figure 2.7, right. The sudden upsurge in force in the results for the bowtie structure seen in Figure 2.6, right, is due the misalignment of rollers inside the test fixture.

2.4.2 Honeycomb arrays

2.4.2.1 Honeycomb arrays with and without defects loaded in X-direction

The second set of tests were conducted for the structures containing primarily honeycomb unit cells, and the results are shown in Figure 2.8 and, Figure 2.9. Substituting in a row of

bowtie repeat units in the honeycomb array makes the structures softer, i.e., less stiff, in both tension and compression when loaded in X-direction as represented by Figure 2.8. Substituting in a column of bowtie units does not necessarily mean that the structure is the most stiff in compression, although it is true for tension in the X-direction as seen in Figure 2.8, left.

2.4.2.2 Honeycomb arrays with and without defects loaded in Y-direction

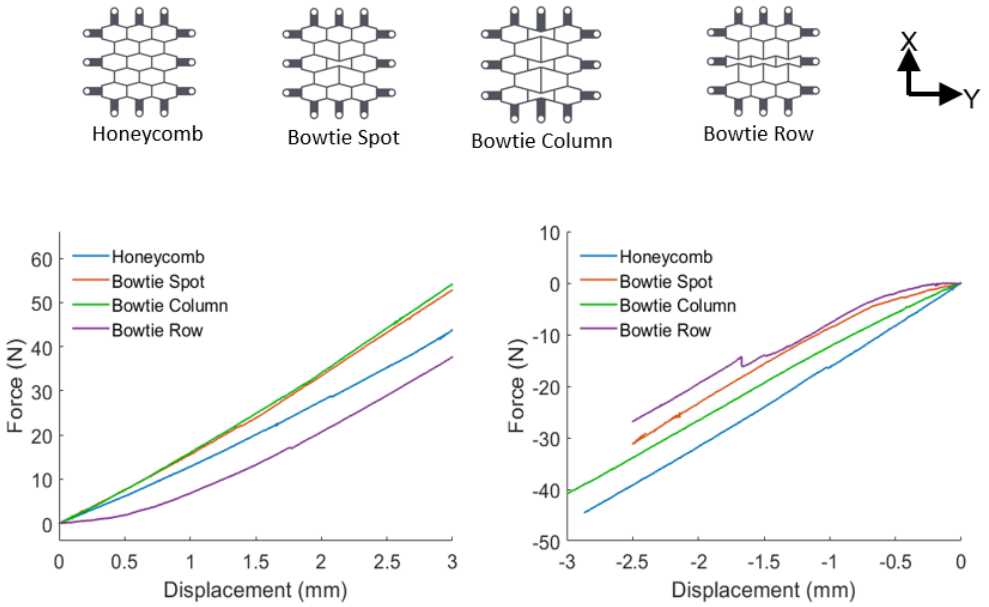

Figure 2.8: Force-displacement curves for honeycomb structures loaded in the X-direction: (left) in tension and (right) in compression.

Adding a row of bowtie elements in the honeycomb array makes the structures softer, i.e., less stiff, when loaded in the Y-direction in both tension and compression, as seen in Figure 2.9. However,the stiffness of the bowtie row array surpasses the bowtie column array beyond a compression of 2.1 mm in the Y-direction. Adding column of bowtie elements as a defect makes the structure more stiff in tension in the X-direction, as seen in Figure 2.9, left, but not in compression.

2.5 Conclusion

This chapter experimentally investigated two-dimensional, polymer based mechanical metamaterials. Lattice structures consisting of honeycomb and bowtie repeat units were printed with

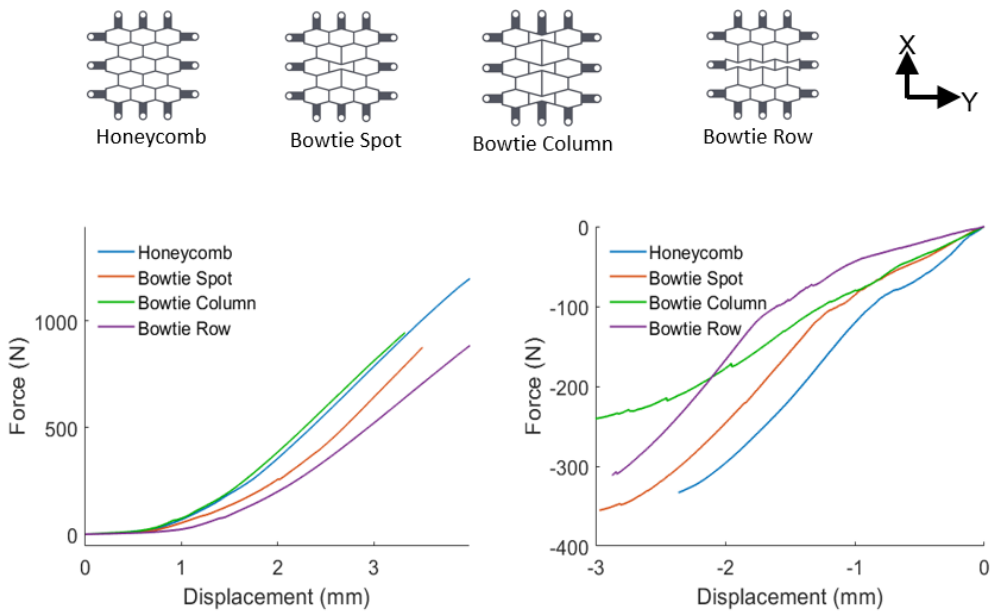

Figure 2.9: Force-displacement curves for honeycomb structures loaded in the Y-direction: (left) in tension and (right) in compression.

PLA in a Makerbot Replicator+, which uses FDM. A custom test fixture was designed and constructed to test the lattices. The effects of friction were highly reduced by the use of rollers for mounting the lattices to the test fixture. The samples were subjected to tension and compression loading to investigate the mechanical behavior of the lattices and the effect of defects on primarily bowtie and honeycomb structures.

The results indicated a fairly linear response for lattices loaded in the X-direction, as loading in the direction transverse to the diagonal ligaments caused these regions to bend with a spring-like behavior. Nonlinear force-displacement results in the Y-direction result from loading along the direction of the diagonal ligaments, which caused these regions to rotate into alignment with the loading direction before stretching. This study showed that the stiffness of the system can be tuned by adding defects and changing the loading direction of the system. For the geometries tested, the bowtie element is more compliant in the Y-direction, due to the higher angle of inclination of the diagonal ligaments. Introducing a column of defects was found to have increased the system stiffness (except in X-direction for bowtie arrays with defects). On the other hand introducing a row of defects in a bowtie array decreased the system stiffness. This study elucidates the effects of geometry and defects on the tunable stiffness of

the lattice arrays for specific applications such as energy absorption, dissipation, and tunable Poisson's ratio.

The structures presented in this Chapter returned to their initial state after the tensile force was removed. The design and testing of these structures triggered a question: Can we design and analyze lattice structures that can remain in the deformed state even after the removal of the tensile force? Next two chapters are answers to this question.

Chapter 3

Bistable Planar Structure

3.1 Abstract

Advances in additive manufacturing have resulted in the ability to accurately produce lattice structures with novel mechanical properties. For example, the incorporation of bi-stable elements, e.g. chevrons and sinusoidal beams, and the use of flexible polymers, e.g. thermoplastic polyurethane (TPU), enable lattices with multiple stable states. The ability to print these structures to conform to non-planar surfaces further complicates the mechanical behaviors of the lattices. Previous studies have focused on planar lattice structures with multiple stable states and on auxetic lattices, i.e. structures with negative Poisson's ratio. Herein, we investigate experimentally the axial mechanical behavior of multi-stable lattice structures based on the printing configuration. Repeat units of the lattice are printed using fused deposition modeling (FDM) with various number of repeat units which are tested under uniaxial tension and compression loads. Further, we evaluate the effects of the initial printing configuration (e.g. extended or collapsed), the shape of bi-stable elements and, the number and size of repeat units on the mechanical behavior of the lattice structures. The results provide insight into the mechanical behavior of mulitstable planar lattices, which have application in impact absorption, vibration damping, and reconfigurable structures.

3.2 Introduction

As discussed in Chapter 1, mechanical metamaterials, which acquire their properties from the geometry rather than their composition, have gained great interest due to their unique and tailored mechanical properties [8–10, 25]. Structures with regular repeat units based on elastic buckling exhibit desirable properties such as high energy absorption [11–15], vibration isolation [16, 17], shock absorption [19, 20], bistability [91]. Bistable metamaterials have two stable states and tessellation of bistable unit cells can be used to achieve multistable metamaterials. Bistable metamaterials possess domains of negative stiffness,i.e., the structure continues to deform under decreasing force, offer high energy absorption, and are able to undergo significant changes in shape without plastic deformation. These properties make bistable structures a suitable alternate for traditional energy absorption structures, which perform their function only once and are not reusable.

Most recently, bistable metamaterials have been exploited with novel 2D and 3D configurations to create recoverable energy absorbing materials in elastic systems. The current studies have focused on analyzing the mechanical behavior of collapsed (closed) configuration of bistable structures. In spite of these studies, the study of their mechanical behavior when fabricated in different configurations remains unstudied. In this chapter, the mechanical behavior of various combination bistable planar metamaterials fabricated in collapsed (closed) and expanded states (open) is investigated.

3.3 Fabrication

The planar structures were additively manufactured in the polymer Thermoplastic Polyurethane (TPU) via Fused Deposition Modeling (FDM). The parts were modeled using Computer Aided Design (CAD) and printed using Prusa i3MK3s printer. The infill density of the print was 100%.

The mechanical response of the base material was characterized with uniaxial loading of a dog bone sample of TPU printed with filaments along the loading direction. The initial

elastic modulus of the base material was obtained approximately as 100 GPa from the uniaxial stress-strain curve shown in Figure 3.1.

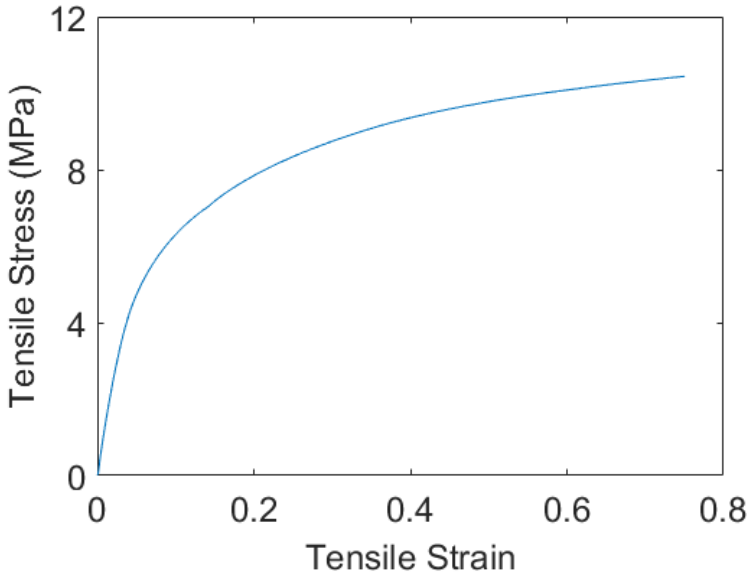

Figure 3.1: Stress- Strain curve for dogbone sample of TPU

3.4 Design of repeat unit geometry

The basic design of a single bistable repeat unit cell is shown in Figure 3.2 (a) . It consists of a sinusoidal beam along with its mirrored image about the central horizontal axis. These two snapping elements are centrally clamped to relatively stiffer supporting segments. When we tessellate this repeat unit together with other repeat units, the thick bars overlap at the central dashed white line. This repeat unit geometry is incorporated into larger lattice array as shown in Figure 3.2 (b), where the single repeat unit is highlighted in green. The repeat unit can be tessellated or patterned horizontally to obtained individual rows (shown in yellow) or vertically to obtain columns (shown in blue). The nomenclature is such that, for instance, the yellow box represents 1 row and 3 columns.

The lattice structures that are discussed above are in collapsed state but these structures can also be designed in expanded state as shown in Figure 3.3. All the geometric parameters are the same except the re-entrant sinusoidal beam is replaced by expanded beam.

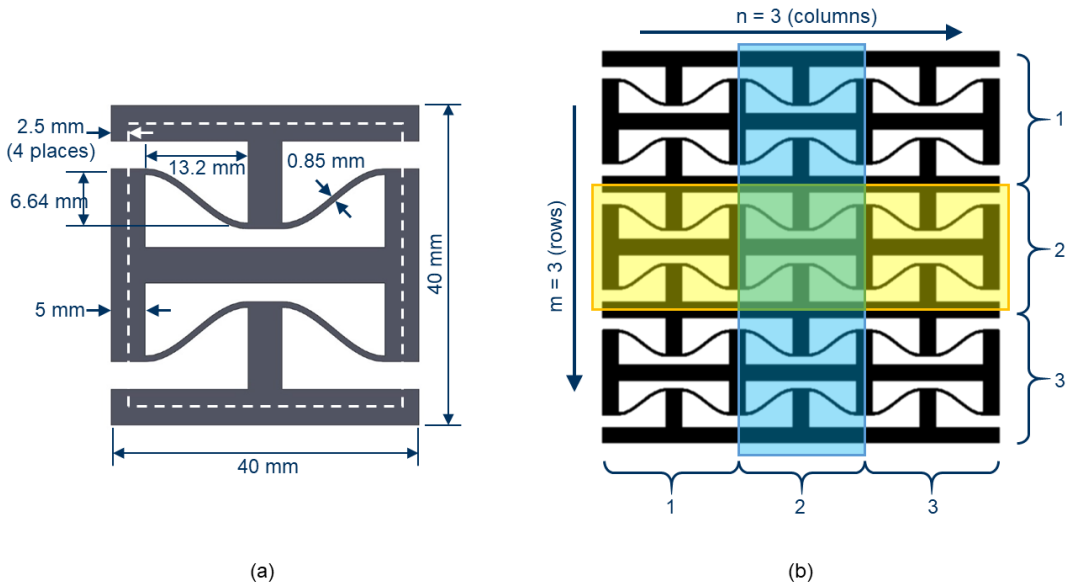

Figure 3.2: Collapsed state (a) single repeat unit geometry with all the necessary dimensions used for 3D printing (b) unit cell arranged in an array of three rows and three columns

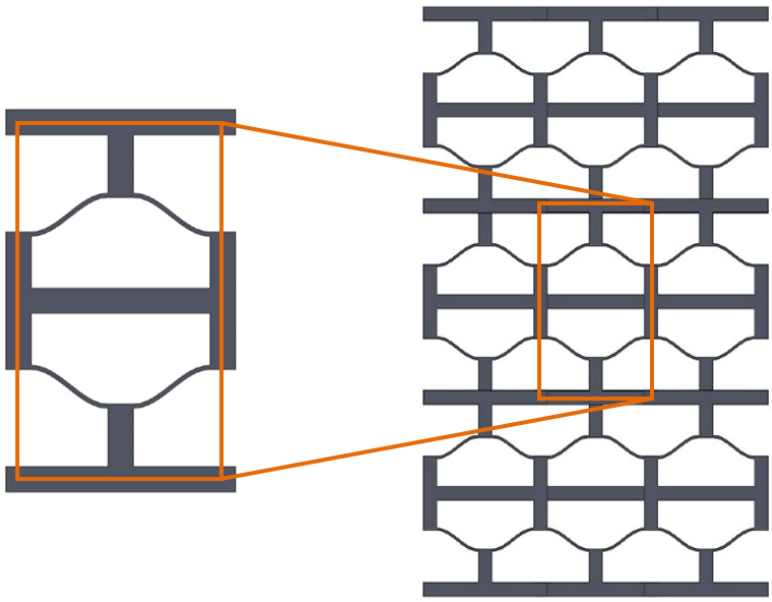

Figure 3.3: Bistable repeat unit in expanded state (left) and unit cell arranged in an array of three rows and three columns (right)

3.5 Experiment

The force - displacement relationships for investigating the mechanical behavior, was studied by conducting tension and compression tests in an Instron 5565 with a 1 kN load cell. Tests

were conducted under displacement controlled cross-head speed of 50 mm/min at room temperature.

3.6 Results and Discussion

Various combination of bistable lattices were printed in collapsed and expanded configuration whose results are presented and discussed below:

3.6.1 Bistable lattices printed in collapsed configuration

The first set of results were obtained for planar lattices printed in collapsed configuration. For this, two sets of experiments were conducted. First set of tension and compression were performed with lattices that were printed in collapsed configuration and initially subjected at collapsed state. The results are shown in Figure 3.4. For 1*1 array shown in blue, there are two local maximum and minimum which correspond to two snap-through. After both have snapped - through in tension to the expanded state, there is rapid increase in the force required to further expand the lattice unit. Similar result is seen for a single row with three repeat units patterned horizontally. For a single column of three repeat units stacked on top of each other, the local maximum and minimum of the snap-through phenomenon are not clear. This is attributed to the rotating of the repeating units as the structure is pulled along the column direction. Finally, for the 3*3 array, six local maximum and local minimum are clearly seen, corresponding to the snap-through of sinusoidal beam in each layer.

Next set of tests were performed in lattice that were printed in collapsed configuration but initially held at expanded state prior subjecting the lattice to compressive load, refer Figure 3.5. For 1*1 and 1*3 results, we see a similar trend as discussed earlier with two clear local maximum and minimum corresponding to the snap through of sinusoidal beams. For 3*1 array, we do not see a clear trend of local maximum and minimum because of the rotation caused by the repeat units along the column. For 3*3 array, there are six local maximum and minimum corresponding to snap-through of each repeat unit both at the top and bottom of sinusoidal beams.

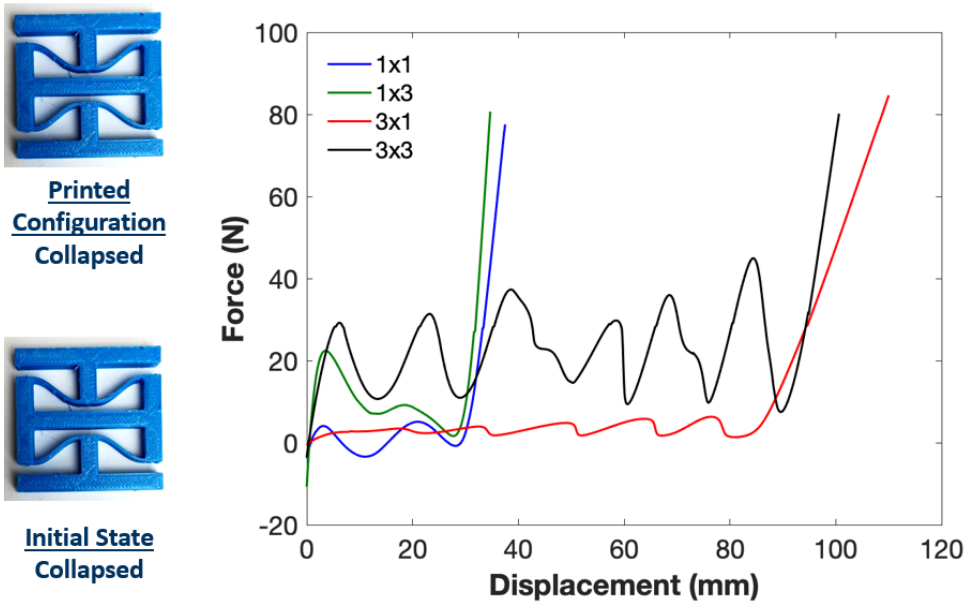

Figure 3.4: Mechanical response of bistable lattices printed and tested in collapsed configuration for the lattices with number of rows and columns varying from 1*1 to 3*3

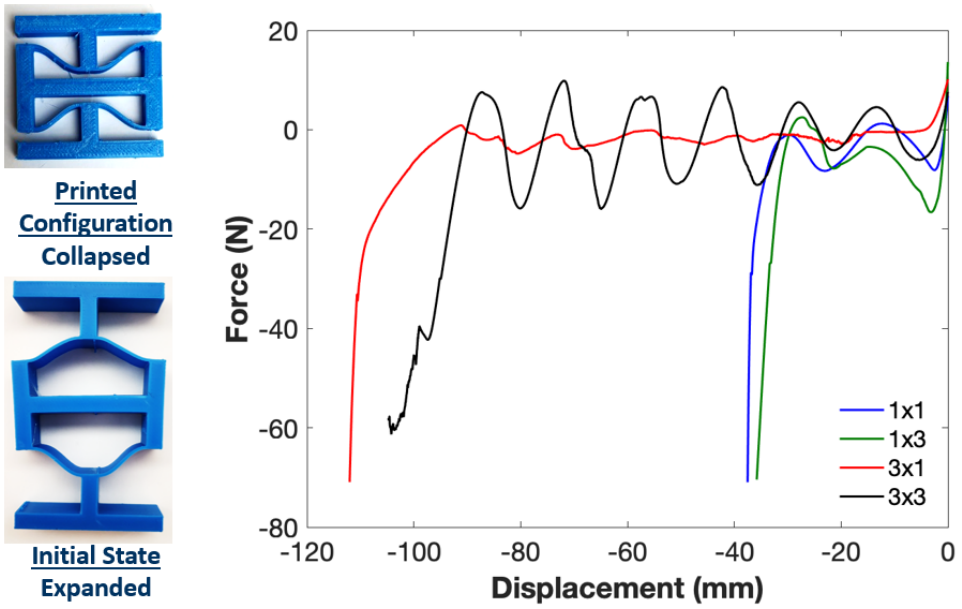

Figure 3.5: Mechanical response of different bistable lattices printed in collapsed configuration but tested in expanded state for the lattices with number of rows and columns varying from 1*1 to 3*3

3.6.2 Bistable lattices printed in expanded configuration

Next set of tests were performed in the lattice that were initially printed in expanded configuration and placed in collapsed state prior to testing, refer Figure 3.6. Similar to the first set of results discussed earlier, we see similar trends with 1*1 and 1*3 where the 1*3 has the higher

force required to initiate the snap-through due to the three repeat units. For 3*1, the local maximum and local minimum are more clear compared to the previous results. For 3*3, the peaks for each of the sinusoidal beam snap-through is slightly different.

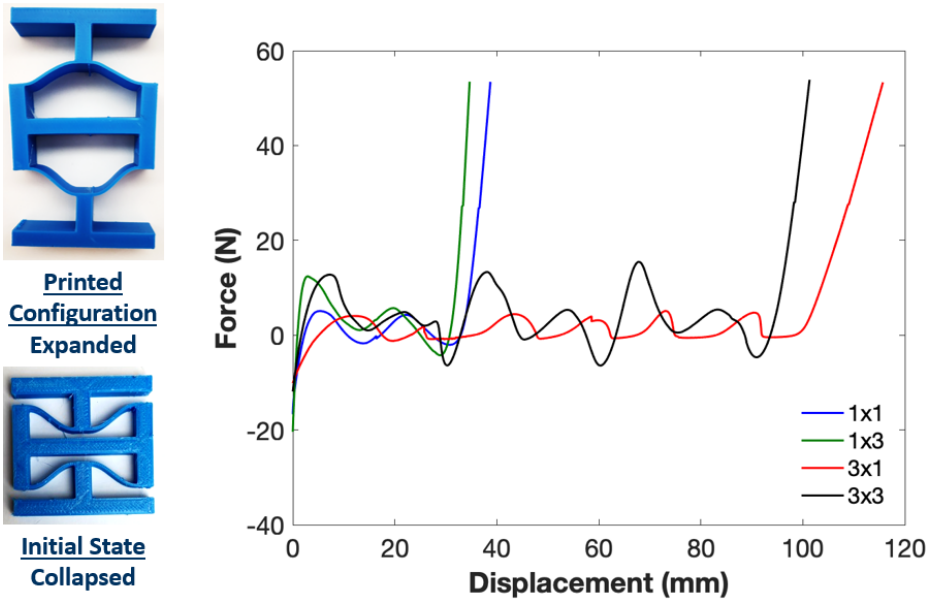

Figure 3.6: Mechanical response of different bistable lattices printed in expanded configuration and tested in collapsed state for the lattices with number of rows and columns varying from 1*1 to 3*3

The last permutation for the test was performed on lattices printed in expanded configuration and subjected to expanded state prior to testing, refer Figure 3.7. We see similar trend as on the Figure 3.6 where 1*1 and 1*3 have very similar local maximum and minimum. The results for 3*1 still has unclear local maximum and minimum because of the rotation of the repeat units along the column. Also, the magnitude of snapping force for 3*3 varies as the snapping progresses.

3.7 Conclusion

We experimentally investigated bistable lattice structures. Lattice structures were fabricated using additive manufacturing. We used TPU which enabled flexible bistable structures. The lattices were subjected to compressive and tensile mechanical displacements under displacement control.

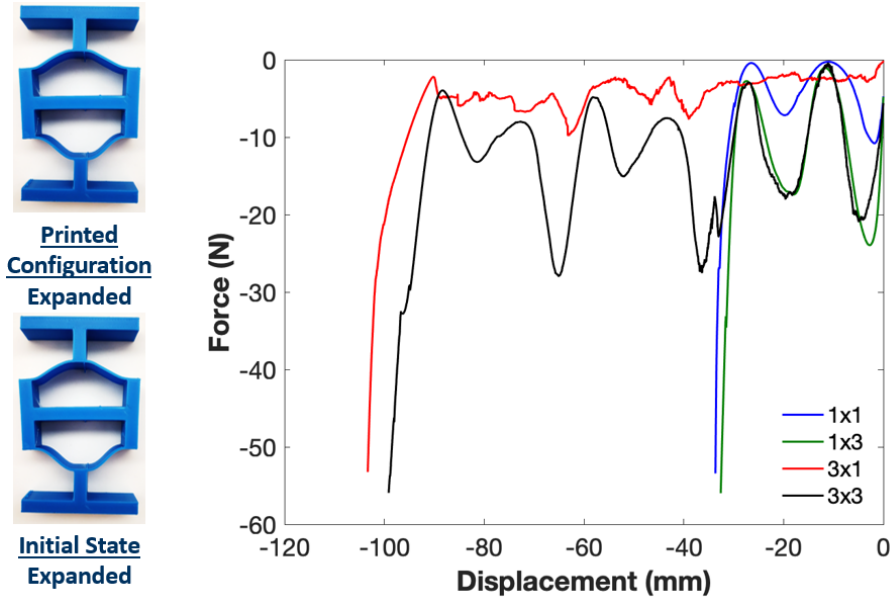

Figure 3.7: Mechanical response of different bistable lattices printed and tested in expanded configuration for the lattices with number of rows and columns varying from 1*1 to 3*3

The bistable structures exhibited non-linear mechanical response. Force-displacement relationships indicate dependence on number of repeat units, printed configuration and initial state. All the lattice structures exhibited clear bistable behavior except for a column of 3*1 because of the rotation of the repeat units. These tests and results motivated us to look at the more complex geometries of the multistable structures like cylinders which is discussed in the next chapter.

Chapter 4

Multistable Cylindrical Metamaterial

This chapter was originally published in International Journal of Mechanical Sciences [64].

4.1 Abstract

Mechancial metamaterials comprising bistable unit cells utilize a sinusoidal beam to enable significant deformation between stable states, which is associated with energy absorption. A stack of similar bistable unit cells, i.e., multistable metamaterials, will snap to a second stable state in a seemingly random sequence that is influenced by minute variations in manufacturing. However, it is desirable to tailor the energy absorbed and the snapping sequence to obtain predictable geometric reconfiguration in multistable cylindrical metamaterials. AM processes, such as FDM, are able to produce these structures with flexible filaments, such as TPU, to enable flexible, multistable cylindrical structures. In this study, we investigated experimentally and computationally the mechanical behavior and controlled snapping sequence of bistable lattices incorporated into cylindrical shells. Individual layers are printed using FDM and assembled into a cylinder. Experimental and computational results for uniaxial tension and compression tests, applied along the length of the cylinder, are used to evaluate the non-linear mechanical behavior and quantify energy absorption of the system during both loading (tension) and unloading (compression). It was shown that energy absorption during loading was always greater than unloading and increased with an increasing number of layers. The energy absorbed by individual layer was approximately 1.25 J in loading and 0.52 J in unloading for a layer with sinusoidal beam thickness of 1.5 mm. The direction dependence of the energy absorption is attributed to the printed configuration of the lattices. Individual layers can be stacked

to tailor the amount of energy absorption. In addition, the energy absorbed and the snapping sequence of the multistable cylinder could be controlled by changing the thickness of the sinusoidal beams in each layer. The variation of energy absorbed is strongly influenced by the thickness of the sinusoidal beam. By increasing the beam thickness from 1 mm to 2 mm, energy absorption increased by approximately a factor of three. Beam thickness accurately controlled the snap-through behavior in experimental samples, but the computational model experienced re-distribution of strain and snap-close forces that cause less predictable snap-through behavior in unloading (compression). The design, analysis and control of snapping sequence of cylindrical shells with multistable states provides new opportunities in practical application of control of elastic waves, energy absorption and reconfigurable structures.

4.2 Introduction

Mechanical metamaterials are engineered structures with properties not found in naturally occurring materials. These materials acquire their unique properties from structure rather than the composition of their internal constituents [8–10]. Structures with regular repeat units possesses desirable properties such as high energy absorption [11–15], vibration isolation [16–18], shock absorption [19, 20], highly sensitive sensors [21–23] and seismic wave protection [24]. Further, the geometry of the unit cell can be designed to obtain unconventional properties such as bistability [25, 26], negative Poisson's ratio [27–29], negative compressibility [8, 30] and extremely lightweight with high stiffness [31]. Bistable metamaterials possess domains of negative stiffness, offer high energy absorption, and are able to undergo significant changes in shape without plastic deformation. These properties make bistable structures a suitable alternate for traditional energy absorption structures, which perform their function only once and are not reusable [26, 92]. Previous studies have focused on planar bistable lattice structures, but advances in additive manufacturing [93, 94] have lead to the incorporation of bistable unit cells into non-planar structures, such as multistable cylindrical shells [95–100].

Bistable structures incorporate mechanical instabilities, such as buckling or snap-through, to transition the structure to its second stable state. Mechanical instabilities enable energy absorption by imparting the structure with domains of negative stiffness, i.e., the structure continues to deform under decreasing force. Negative stiffness is achieved when beams are subjected to loading such as compression and bending [101]. One such structure that demonstrates bistability is the doubly curved sinusoidal beam constrained at both ends. Sinusoidal beams enable bistable behavior without the use of latches, hinges, or residual stress [25]. Qui *et al.* [25] investigated the buckling behavior of sinusoidal beams for application in microelectromechanical systems (MEMS) components such as relays, valves, clips, threshold switches and memory cells. Analytical results indicated that bistability requires a critical ratio of beam amplitude to thickness, termed the geometric parameter, Q. The resulting structures were stable in two configurations and thus did not rely on hinges or latches. Further studies proposed quantitative analytical and theoretical models aimed at tailoring the snap-through behavior of the curved beams using an array of bistable lattice structures [26, 102–104]. For instance, Phase Transforming Cellular Structures (PTCS) comprise compliant planar bistable or metastable mechanisms that enable the structures to switch between multiple stable configurations [26, 63, 105], and Shan et.al [63] designed a reusable material with controlled trapping of elastic energy which possessed bistable elements. In all of the PTCSs, transition from one stable phase to another stable phase is achieved via deformation of the bistable elements which exhibit negative stiffness during snap-through [26].

Bistable lattices in one-, two-, and three- dimensions were studied analytically and experimentally in terms of mechanical response [26], thermal behavior [106], dynamic behavior [103], wave propagation [107], deformation sequence [108], magnetic multistable metamaterial [109], rotational multistability [110], and morphing applications [111]. Previous studies investigated the effects of small geometric variations [108], Young's Modulus variation [112], temperature dependence [106], and fiber reinforcement [113] on snapping of planar bistable lattice structures. Recently, theoretical and analytical analysis of cylindrical structure with multistable states has been performed to propose the criteria for bi-stability of cylindrical layers [95]. These authors fabricated multistable cylindrical shells and showed that the force–displacement

response under sequential loading and unloading formed a hysteresis loop, which indicated the structure was able to absorb and dissipate energy. Scholars also investigated the influence of the number of unit cells in each layer and the unit cell geometric parameter, Q (introduced earlier), on the mechanical response for a single layer for planar and cylindrical metamaterials [96]. However, the sequence in which individual layers of the multistable cylindrical shells deform, which we will call guided snap-through behavior, has not been investigated. Further, the influence of number of layers and changing beam thickness to tailor the energy absorption of cylindrical shell metamaterials has not been investigated. Such development is thus the focus of the current investigation, where the novel contribution lies in the determination of the controlled energy absorption and snapping sequence which is desirable in several applications such as control of propagation of elastic waves [114–117] and deployable and morphing structures [118–123]. Cylindrical structures have numerous applications in mechanical engineering, including from morphing skins in airspace industry [124, 125]. In addition, the incorporation of bistable structures into cylindrical shells can be used in heat redistributing tubes in air conditioning and bio-medicine such as stents, and catheters [125].

In this study, we investigate the effects of varying the number of layers and thickness of the sinusoidal beams on the energy absorption and snapping/deformation sequence of a multistable, cylindrical shell. Two types of multistable cylindrical layers were fabricated using FDM and their mechanical behaviors and energy absorption were measured and discussed. Finally, the thickness of the bistable, sinusoidal beams in each layer was used to guide the sequence of snap-through responses in the cylinder. Experimental results are compared to analytical and finite element models to provide additional insight into the behavior of the multistable cylinders. This investigation contributes insight into the behavior of bistable unit cells incorporated into the walls of cylindrical structures. We study the mechanical behavior of the cylinders in both loading (tension) and unloading (compression) and quantify the energy absorption during deformation. Additionally, we investigate techniques to tailor the energy absorption and snapping sequence of multistable cylinders.

4.3 Materials and Methods

In this section, the mechanical response of a bistable unit cell configuration is discussed in Section 4.3.1. This is followed by the discussion of important parameters to consider while designing bistable structures in Section 4.3.2 The design parameters of bistable cylindrical structures are mentioned in Section 4.3.3. The fabrication and experimental techniques are briefly discussed in Section 4.3.4 and Section 4.3.5, respectively. The Finite Element Analysis (FEA) methodology is explained in Section 4.3.6. Lastly, the material model is presented in Section 4.3.7.

4.3.1 Design of Bistable unit cell

The multistable cylindrical structures presented here consists of an array of bistable unit cells. The mechanics of planar bistable unit cells have been proposed in the previous studies [25, 26]. The shape of the curved beam as shown in Figure 4.1a can be represented by the equation $y = \frac{h}{2}[1 - cos(\frac{2\pi x}{l})]$, where h is the amplitude of sine wave and l is the span of the curved beam. If we consider the vertical displacement d with the application of a concentrated force f, the behavior of the elementary beam can be studied as shown in Figure 4.1b. As the beam deforms from the initial stable configuration ($d = 0$) to second stable configuration ($d = 2h$) the force-displacement curve can be divided into three regions:

- **State 1:** $0 \leq d \leq d_1$: elastic deformation until $f = f_{max}$ (positive stiffness)
- **State 2:** $d_1 < d < d_2$: snap-through deformation until $f = f_{min}$ (negative stiffness)
- **State 3:** $d_2 \leq d \leq d = 2h$: elastic deformation (positive stiffness)

The total potential energy U has three noticeable points:

- $(d = 0, f = 0)$: undeformed (stable)
- $(d = h, f = 0)$: maximum strain energy (unstable)
- $(d = 2h, f = 0)$: local minimum strain energy (stable)

State 1 and state 3 represent stable states, wherein increased force is required to increase displacement, *i.e.,* the regions of positive stiffness. Reduction of the force in these states results in the sample returning to a stable configuration. State 2 represents the transition of the bistable mechanism between stable State 1 and stable State 3, which is indicated by a region of negative stiffness. As the transition state, State 2 has the highest strain potential energy and a state transformation point at $d = h$. At this point, the structure is most unstable, and release of the structure will result in immediate switching to stable State 1 or stable State 3.

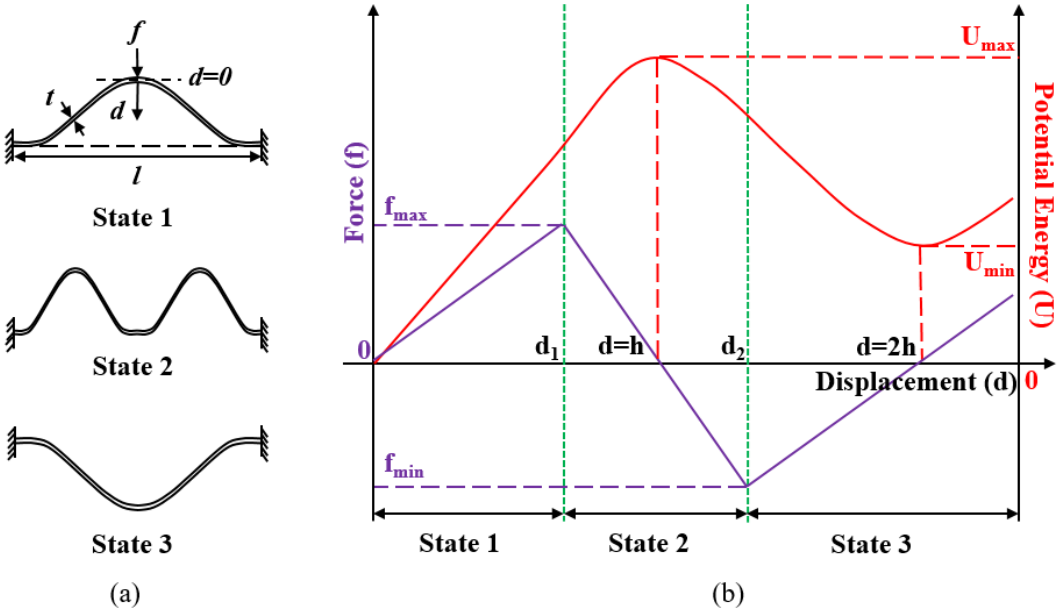

Figure 4.1: Mechanical response of a curved beam (a) Curved beam with span l, thickness t, applied force f and its three different states after the application of transverse force f. The structure is stable in State 1 and State 3. The beam takes on an unstable, buckled configuration in State 2. (b) Force-displacement and potential energy-displacement response for a bistable beam in three different states.

4.3.2 Relation between F and Q

The snap-through of the bistable beam enables the unit cell to absorb energy without undergoing plastic deformation. When the two ends of the beam segment are constrained, the transverse (vertical) displacement of the center of a curved beam is related to the transverse (vertical) force applied to the center of a beam for the three modes, refer to Figure 4.2a, respectively, are as follows [25]:

$$F_1 = \frac{3\pi^4 Q^2}{2}\Delta\left(\Delta - \frac{3}{2} + \sqrt{\frac{1}{4} - \frac{4}{3Q^2}}\right)\left(\Delta - \frac{3}{2} - \sqrt{\frac{1}{4} - \frac{4}{3Q^2}}\right) \tag{4.1}$$

$$F_2 = 4.18\pi^4 - 2.18\pi^4\Delta \tag{4.2}$$

$$F_3 = 8\pi^4 - 6\pi^4\Delta \tag{4.3}$$

where F_i and Δ are normalized force and normalized displacement variables, respectively. The normalized variables are related to the applied transverse force f and transverse displacement d as follows:

$$F_i = \frac{f_i l^3}{EIh}, \qquad \Delta = \frac{d}{h}, \qquad Q = \frac{h}{t} \tag{4.4}$$

where E and I are the modulus of elasticity of the cell wall and second-area moment of inertia, respectively. The important parameter here to obtain bistability from snap-through is Q which is the ratio of the amplitude of the sine wave h to thickness of curved part of beam t. Figure 4.2b shows a plot of equations 4.1, 4.2 and 4.3. F_2 and F_3 are straight lines with a negative slope that do not depend on Q whereas F_1 depends on Q. In this plot, bistability is realized when $F_i \leq 0$ for normalized displacement $\Delta > 1$. When $Q < 2.31$ the planar beam has just one stable state, and when $Q \geq 2.31$ the planar beam has two stable states with a region of negative stiffness from approximately $0.5 < \Delta < 1.5$. In realistic tests of bistable structures, the force displacement curve will transition between F_1, F_2, and F_3, depending on the current mode shape. For instance, at Q=10.08, the relationship between normalized force and displacement starts from $\Delta = 0$ and follows the F_1 curve. Depending on the buckling mode, refer to Figure 4.2a, it switches to either the F_2 curve (second mode) or the F_3 curve (third mode, which is equivalent to shape during State 3, Figure 4.1a), both of which have a negative slope. The curve then rejoins F_1 curve before reaching the second stable state at $\Delta = 2$. The values of Q chosen for the present study vary from 7.56 to 15.12, all of which exhibit bistability [95]. The peak and bottom forces, when the second mode is constrained, are approximated by the dimensionalized forces:[25]:

$$f_{3(peak)} \approx 8\pi^4\frac{EIh}{l^3}, \qquad f_{3(bottom)} \approx 4\pi^4\frac{EIh}{l^3} \tag{4.5}$$

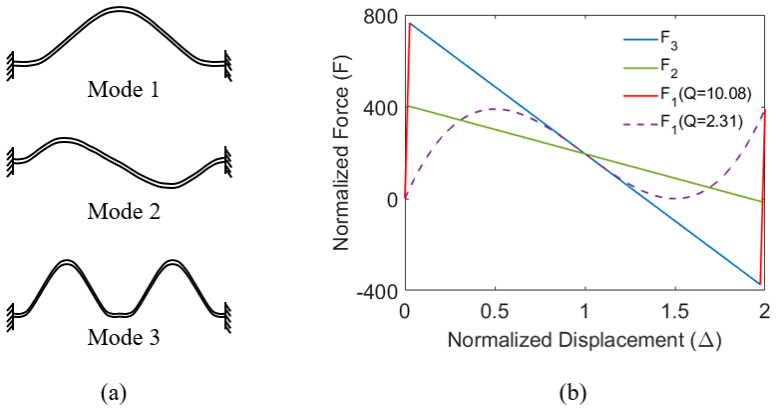

Figure 4.2: (a) Three buckling modes of a curved beam constrained at both ends. Mode 2 and Mode 3 are possible mode shapes during the unstable State 2. (b) Normalized force versus normalized displacement for three different modes. F_2 and F_3 are straight lines with a negative slope that do not depend on Q. Bistability is attained at Q=2.31, shown for reference.

4.3.3 Design of Cylindrical Bistable Structures

The design of our bistable structure is inspired by previous studies, which used planar arrays of bistable cells [26, 91, 108]. The bistable unit cells in each cylindrical layer were designed

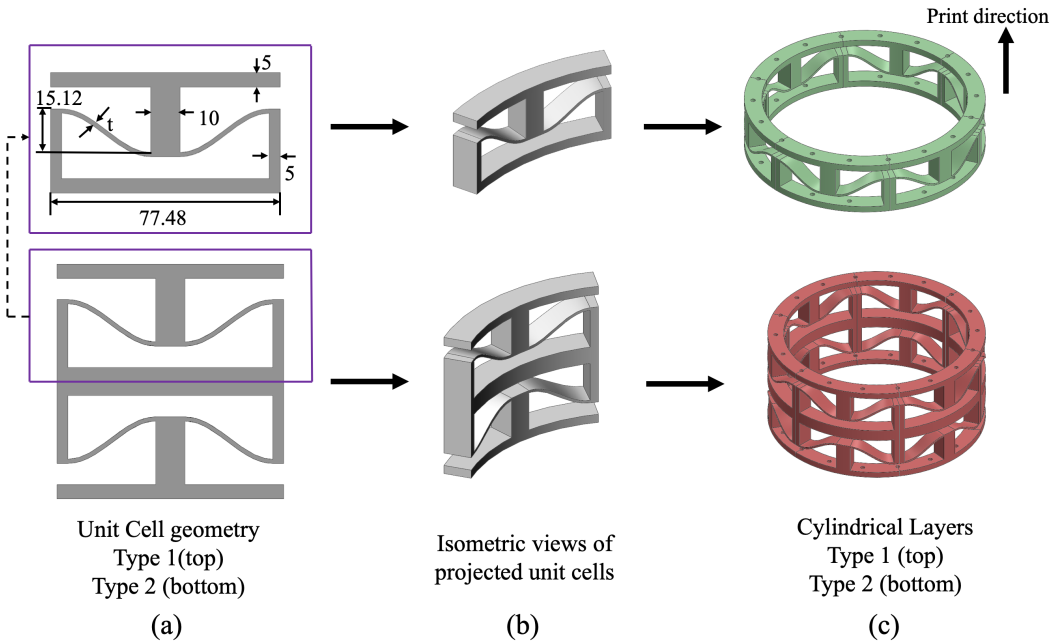

Figure 4.3: Geometries of basic unit cells for Type 1 (top) and Type 2 (bottom) multistable cylinders. (a) Dimensions of planar unit cells (units in mm). (b) Unit cells projected onto a cylinder with a radius of 74.2 mm and extruded 12.7 mm outward to obtain a cylinder with an outer radius, R = 86.69 mm. (c) Arrays of six unit cells patterned around the cylinder. The orientation of the structure during 3D printing is indicated by the arrow in the upper right-hand corner.

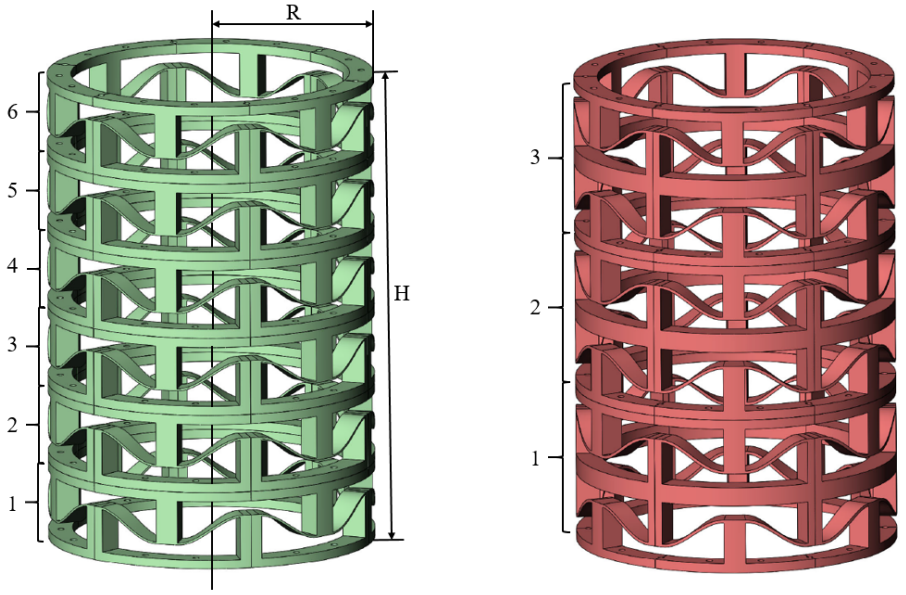

Figure 4.4: (a) Cylinder comprising six Type 1 layers (1-6) with outer radius R, and height H. (b) Cylinder comprising three Type 2 layers (1-3) with same radius R and height H as in (a).

in the closed, or collapsed, configuration as shown in Figures 4.3 and 4.4. Dimensions for the printed structures were selected based on the minimum print resolution and maximum build volume of typical FDM printer. Thicker vertical stems aid in replicating the fixed constraints at the ends of the beams and partially restricts the second (asymmetric) buckling mode. Further, higher Q values (h/t) ensure clear bistable behavior and have remained largely unstudied in the literature. Sketches of the basic bistable unit cells are shown in Figure 4.3a, where t is the thickness of the sinusoidal beam which is taken initially as $t = 1.50$ mm for all layers while investigating the mechanical behavior and energy absorption. Additional layers were modeled in which the thickness was varied from 1 mm to 2 mm, with an increment of 0.2 mm, to study the effects of beam thickness on the guided snapping sequence behavior. The wave amplitude is $h = 15.12$ mm and the span of the beam is $l = 77.48$ mm for all geometries. The unit cell with these dimensions was sketched in the 2D plane and projected onto a cylinder with a radius of 74.2 mm, and extruded radially outward by 12.7 mm. The fabricated cylindrical shells therefore have an in inner radius of 74.2 mm and an outer radius (R) of 86.69 mm . The overall dimension of Type 1 unit cell (with one row of snapping elements) was $77.48 \times 41.78 \times 12.70$ mm. This parent unit cell was reflected vertically, as shown in Figure 4.3, bottom, to create the Type 2

unit cell. Thus the height of Type 2 unit cell (with two rows of snapping elements) was twice that of the Type 1 unit cell. The overall dimension of Type 2 unit cell was $77.48 \times 83.56 \times 12.70$ mm. These two types of unit cells were patterned as an array of six unit cells around a cylinder which formed radius (R) of 86.69 mm as shown in Figure 4.3c. Individual layers were stacked to form the full cylinder as shown in Figure 4.4. The overall height, H, of both Type 1 and Type 2 cylinder after stacking was kept same with a value of 250.68 mm. For the same height, H, of both types of cylinders, there are six individual Type 1 layers, labeled as 1-6, or three Type 2 layers, labeled as 1-3, as shown in Figure 4.4.

4.3.4 Fabrication

All the designs mentioned above were modeled in a 3D computer aided design (CAD) software and converted to a 3D Manufacturing Format (3MF) file for slicing using PrusaSlicer . The structures were then printed with flexible TPU filament using FDM (Prusa i3MK3s) with infill of 100%. TPU was selected for its excellent flexibility and durability, which enable the snap-through behavior at room temperature. Six layers of Type 1 unit cells and three layers of Type 2 unit cells were printed individually, as shown in Figure 4.3c. Layers were printed individually due to the build volume of the 3D printer and to enable a modular study of the metamaterial cylinders. The layers were stacked to form multistable cylinders and fastened with 3.5mm screws. Twelve screws (2 screws per unit cell and 6 unit cells per layer) were used to connect two layers. The center-to-center distance between fasteners was 27.90 mm within each unit cell and 54.95 mm between adjacent unit cells. Eighteen screws at an equal spacing were used on the top and bottom to connect the layers to custom circular test plates (12 mm thick aluminum discs). In addition, a tensile test of the material was performed on three dog-bone specimen according to ASTM D638-14 [126], and the Young's Modulus was obtained to be approximately 100 MPa. The sample was subjected to 700% strain, and the modulus was linear up to 4% strain.

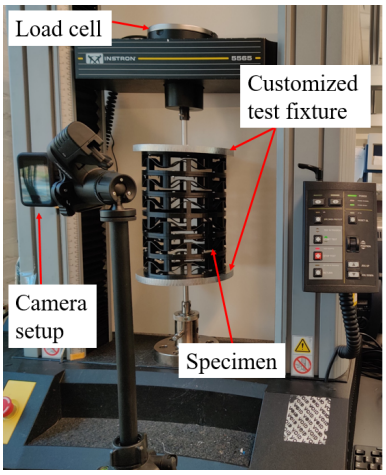

Figure 4.5: Test setup showing the testing machine Instron 5565 with a 1 kN load cell, camera setup, specimen, and the customized test fixture. The custom test fixture consists of 12 mm thick aluminum plates with 12 mm diameter aluminum rods for mounting to the tensile tester.

4.3.5 Experiment

The force - displacement relationships for investigating the mechanical behavior, energy absorption and guided snapping sequence was studied by conducting loading (tension) and unloading (compression) tests with a customized test fixture, shown in Figure 4.5. The test fixture was installed in an Instron 5565 with a 1 kN load cell. Tests were conducted under displacement control at a cross-head speed of 50 mm/min at room temperature. The bistable cylindrical structures were subjected to loading until fully stretched and then compressed back to the collapsed state. Herein, the printed configuration will be referred to as collapsed state and the fully stretched state will be referred as expanded state.

4.3.6 Finite Element Analysis Methodology

The experimental analysis was complemented by a three-dimensional finite element analysis to obtain additional insight into the mechanical behavior of the bistable structures. A dynamic, implicit computational algorithm was used. Dimensions for the finite element model were the same as the models used experimentally to print Type 1 cylinders. The geometries were meshed with tetrahedral elements, and a linear elastic material model with stiffness proportional damping was applied.

Representative finite element models are shown in Figure 4.6. Figure 4.6a shows an isometric view of a single layer, Type 1 cylinder with beam thickness t = 1.5 mm. Figure 4.6b shows an isometric view of a six-layer Type 1 cylinder in which all sinusoidal beam thicknesses are t = 1.5 mm. Boundary conditions for the model are shown in Figure 4.6c. The bottom of each cylinder was pinned to prevent translation, and the top of each cylinder was constrained from motion in the transverse directions. An axial displacement boundary condition was applied to the top of each model in two steps. In step 1, the cylinder was fully extended, and in step 2 the cylinder was returned to its original shape. Throughout this process, the axial reaction forces and the axial displacement at the top of the cylinder were recorded. Separately, the model was analyzed with an additional step between loading and unloading to show that the geometry was bistable after full extension.

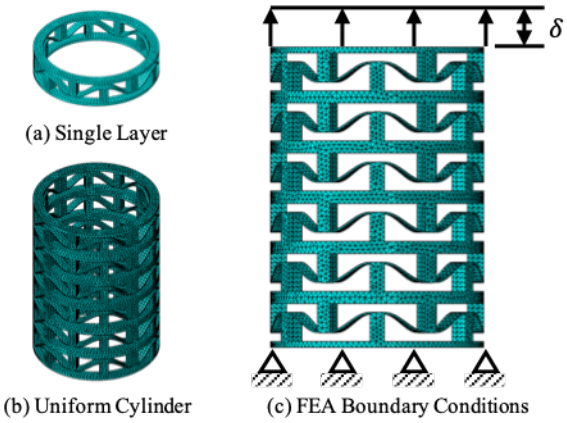

Figure 4.6: Depiction of finite element models. (a) Single layer Type 1 cylinder with sinusoidal beam thickness of t = 1.5 mm. (b) Six-layer Type 1 cylinder with uniform sinusoidal beam thickness of t = 1.5 mm. (c) Depiction of boundary conditions applied to six-layer cylinder. The bottom is pinned in place and the top displaces axially by a prescribed amount, δ. The meshes in all three images were determined by a mesh convergence analysis.

4.3.6.1 Mesh Convergence Analysis for FEA

A mesh convergence analysis was performed on a single, Type 1 layer with beam thickness of 1.5 mm. The global mesh seed was varied to obtain meshes with 1598 (coarse), 3130 (medium), 10597 (medium-fine) and 15054 (fine) elements. Force-displacement results for the various meshes are shown in Figure 4.7. Significant differences in the results are observed as the mesh is refined from coarse to medium-fine. As the mesh is refined from medium-fine to fine, the

changes in the force-displacement curves are less significant. To further evaluate the mesh convergence, the maximum force required to initiate snap-through and the energy absorbed during tension and compression were determined, as shown in Figure 4.8. Significant variation in these parameters is observed from the coarse to medium-fine meshes, and a less significant variation is observed as the mesh is refined to the fine mesh. Therefore, the global mesh seed required for the fine mesh is applied to all models.

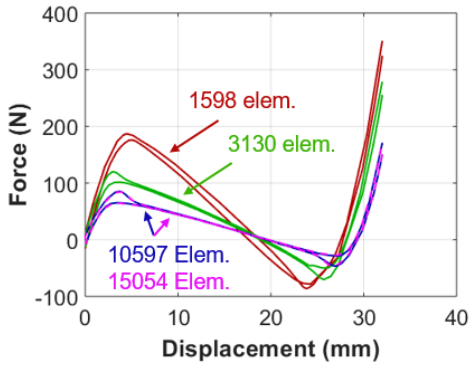

Figure 4.7: Mesh convergence analysis for a single Type 1 layer with beam thickness of 1.5 mm.

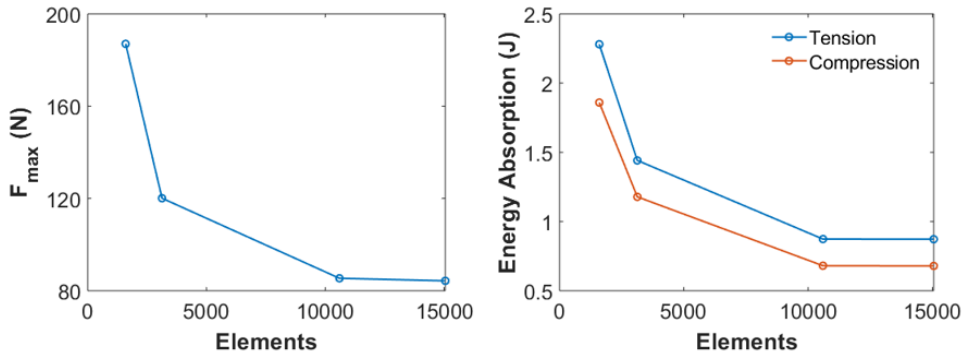

Figure 4.8: Mesh convergence analysis based on maximum force to initiate snap-through (left) and energy absorption (right). The results are for a single Type 1 layer with beam thickness of 1.5 mm.

4.3.7 Material Model

A linear elastic material model with stiffness proportional damping was utilized for FEA. The material modulus, E = 100 MPa, was determined by performing uniaxial tensile tests as described in the experimental section. In addition, the material used to fabricate the metamaterials

was evaluated using differential scanning calorimetry (DSC) and dynamic mechanical analysis (DMA) to characterize the thermomechanical properties.

DSC experiments were conducted using a TA Instruments DSC 25 and utilized a heat-cool-heat sequence between 0°C and 100°C. The results are shown in Figure 4.9. An apparent glass-transition is observed at approximately 55.5°C during the second heating cycle, which is well above the room temperature at which mechanical tests of the metamaterials were performed. Thus, we do not anticipate significant viscoelastic effects.

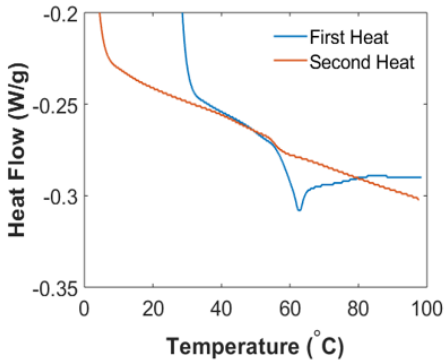

Figure 4.9: Thermogram from differential scanning calorimetry of TPU filament. There is an apparent Tg at 55.5°C during the second heat.

Two DMA experiments were conducted using a TA Instruments DHR-20 with DMA mode using a torsion test fixture to further evaluate any viscoelastic behavior of the material. In the first test, the sample was subjected to a frequency sweep from 0.001 – 100 rad/s at 26°C. The results are plotted in Figure 4.10. These results indicate that the loss modulus, i.e., the damping portion, scales with the storage modulus, i.e., the elastic portion. The average ratio of the loss modulus to the storage modulus is calculated to be β = 0.164, which is taken to be the stiffness proportional damping coefficient used in the computational model. The second DMA experiment was a relaxation test. In this test, the sample is subjected to an initial strain at room temperature, and the stress output is recorded as a function of time. From this, the relaxation modulus is calculated, and the results are shown in Figure 4.11. It is observed that for a timescale from approximately 10^{-2} seconds to $5\text{x}10^{2}$ seconds that the modulus remains largely unchanged, although there is a slight decrease throughout the duration of the experiment. The total time for mechanical tests of the cylindrical structures in the Instron was ≈500 seconds,

and during this time the load in the structure varies constantly. Based on the DMA and DSC results, it is assumed that the material is not viscoelastic, but instead it has some viscous damping behavior in which the damping is proportional to the stiffness of the material. This viscous damping is attributed to a block copolymer structure in the TPU in which the soft phase has a T_g significantly below room temperature and the hard phase has a T_g of approximately 55°C. At room temperature, the soft phase imparts viscous damping to the structure.

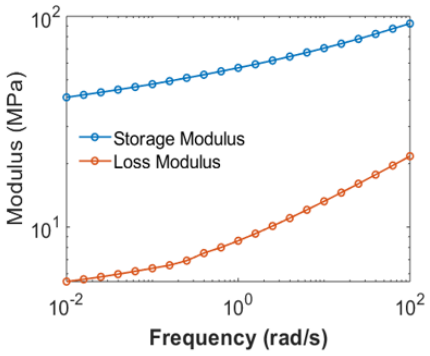

Figure 4.10: Dynamic mechanical analysis (DMA) results for a frequency sweep at 26°C.

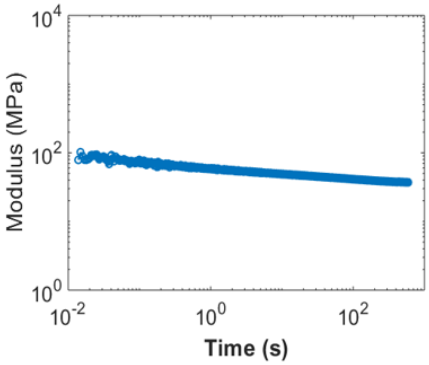

Figure 4.11: Relaxation modulus calculated from relaxation test in DMA.

4.4 Results and Discussion

In this section, results obtained from the sequential loading (tension) and unloading (compression) of cylinders comprising Type 1 and Type 2 layers are discussed. Section 4.4.1 discusses the force - displacement behavior for a varying number of Type 1 and Type 2 layers with constant thickness (1.5 mm) of sinusoidal beam in every layer. Section 4.4.2 analyzes the force - displacement results for energy absorption capacity of the bistable cylindrical structures. It

also discusses the programmability of energy absorption capacity of these structures. In Section 4.4.3, the effects on snapping sequence of varying the thickness of the sinusoidal beams between layers is discussed. Results from the Finite Element Analysis (FEA) are discussed in Section 4.4.4.

4.4.1 Mechanical behavior of Type 1 and Type 2 layers

We first investigated the effects of the number of bistable layers and the type of unit cell used to assemble the cylinders using six Type 1 layers or three Type 2 layers, fabricated separately. The geometric parameters for each unit cell remained constant ($l = 77.48$ mm, $h = 15.05$ mm, $t = 1.50$ mm, and $Q = 10.08$). Recall, the only difference between the two unit cells is that the height of Type 2 layer (with two sinusoidal beam layers) was twice the height of Type 1 (with one sinusoidal beam layer). The force - displacement curve obtained for single Type 1 and Type 2 cylinder layers are shown in Figure 4.13. Each curve is the representative of nine tests performed on the same structure. It is seen that the loading (tension) and unloading (compression) curves do not coincide irrespective of the type of layer. Tests were conducted for a total of 6 Type 1 layers and 3 Type 2 layers. Although this number of specimens represents the total number of layers tested, the assembled structures were each tested in loading (tension) and unloading (compression) a total of 9 times. We also note that the snapping sequence does not follow the same order for each loading and unloading cycle. When the cyclic loading is applied to a single layer consisting of Type 1 unit cells, all of six unit cells around the perimeter of the layer snap at the same time which creates one local maximum and one local minimum force point. Similarly, for an individual Type 2 layer, one half of the layer, *i.e.*, one sinusoidal beam around the cylinder, snaps first, and then the remaining half deforms creating two local maximum and two local minimum force points during loading and unloading. Up to six Type 1 layers or three Type 2 layers (see Figure 4.14) were assembled into cylinders and tested in a similar fashion. The number of peaks and valleys in the force - displacement curves increased with an increasing number of layers. Cylinders comprising Type 1 layers had a number of local maxima and minima forces that corresponded to the number of layers. Type 2 cylinders had twice as many local maxima and minima as the number of layers due to the presence of

two sinusoidal beams within a single Type 2 layer. All cylinders demonstrated a bistable state between snap-through responses.

We observed that the progression of snapping from one layer to another was random when the unit cells in all layers were identical for both Type 1 and Type 2 cylinders. Pictures of a six-layer, Type 1 cylinder with uniform beam thickness of $t = 1.5$ mm are provided in Figure 4.12. In the Type 2 cylinders, there was no sequential snap-through within the two snapping segments of an individual Type 2 layer. In other words, one-half of a layer might snap-through, followed by snap-through of one-half of a different layer. It was observed that the number of snap-through responses depended on the number of layers in the cylinder, but the local maximum and minimum forces were not affected by the number of layers or type of unit cell (Type 1 or Type 2). For cylinders comprising 1 to 6 layers of the Type 1 unit cell, the peak and bottom forces in loading (tension) and unloading (compression) varied from 51 to 68 N and -8 to -15 N, respectively, with an average of 63 N and -12 N. For cylinders comprising 1 to 3 layers of the Type 2 unit cell, the peak and bottom forces in loading (tension) and unloading (compression) varied from 56 to 73 N and -5 to -18 N, respectively, with an average of 63 N and -15 N. The small variations in the local maximum tension and minimum compression forces during loading and unloading is attributed to repeated use of same structure which might introduce residual stress and variations in 3D printing process [26, 127]. Additionally, our use of screws to assemble individual layers may have had a small influence on local maximum and minimum forces. Experimentally, it was observed that the vertical stem in the midspan of the sinusoidal beam tended to constrain the rotation of midspan [128], resulting in a mode shape that more closely resembled that of Mode 3. The magnitude of the expected peak and bottom forces for planar snap-through in loading (tension) and unloading (compression) were approximately 54 N and 27 N, respectively, as obtained using the equation 4.5. The peak and bottom forces obtained analytically using equations 4.5 are in good agreement with the experimental forces which shows that projecting the bistable unit cell onto a cylinder has a negligible effect on the snapping forces. Overall, the mechanical behavior in terms of force and displacement was similar for Type 1 and Type 2 cylindrical layers which had the same value of parameter (Q) and height (h) of 10.08 and 250.68 mm respectively, as evidenced by Figure 4.14. This suggests

that multiple Type 1 layers could be used to estimate the behavior of Type 2 layered structures. Meanwhile, the snap-through process for the structure used here with $Q = 10.08$ is smooth when compared to the experimental results obtained for $Q = 3$ to $Q = 6$ [95] and $Q = 7.5$ [96]. This is attributed to the higher Q value, which leads to a more distinct snap-through behavior, and an increased thickness in the stiffening portions of the unit cell (horizontal and vertical walls).

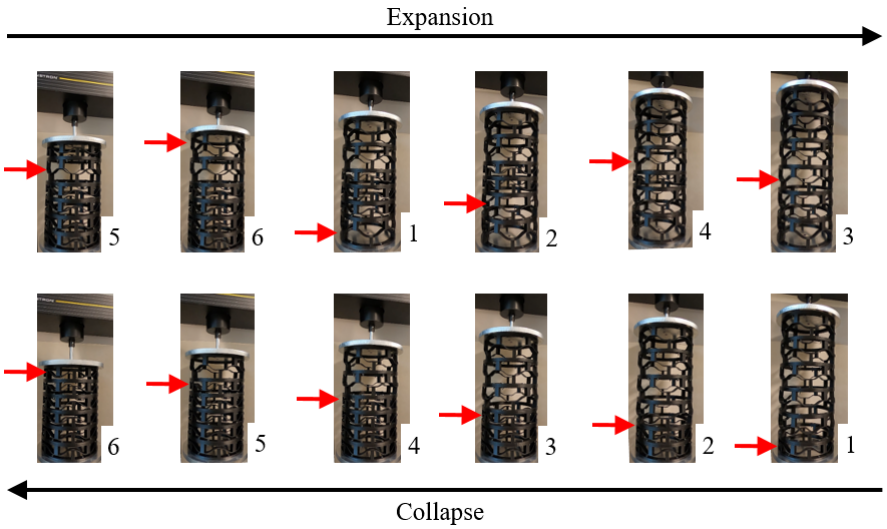

Figure 4.12: Experimental pictures for random snapping sequence when the thickness of sinusoidal beam in all the layers is uniform (1.5 mm).

4.4.2 Energy Absorption of Bistable Cylinders

Next, we evaluated the energy absorption of cylinders comprising one to six Type 1 layers. Only the Type 1 unit cell was considered due to the similarities between the force-displacement curves for the Type 1 and Type 2 cylinders. When Type 1 layers were subjected to sequential loading (tension) and unloading (compression) loading, the loading and unloading curves did not coincide, which resulted in a hysteresis region as evidenced in Figures 4.13 and 4.14. This indicates that these structures are capable of energy absorption. The area under each loading or unloading curve provides a quantitative measure of the energy absorbed by the structure. These parameters are shown schematically in Figure 4.15a. For comparison of energy absorption during loading (tension) and unloading (compression), we separately extracted the data from the collapsed state to the fully expanded state and the fully expanded state to the collapsed

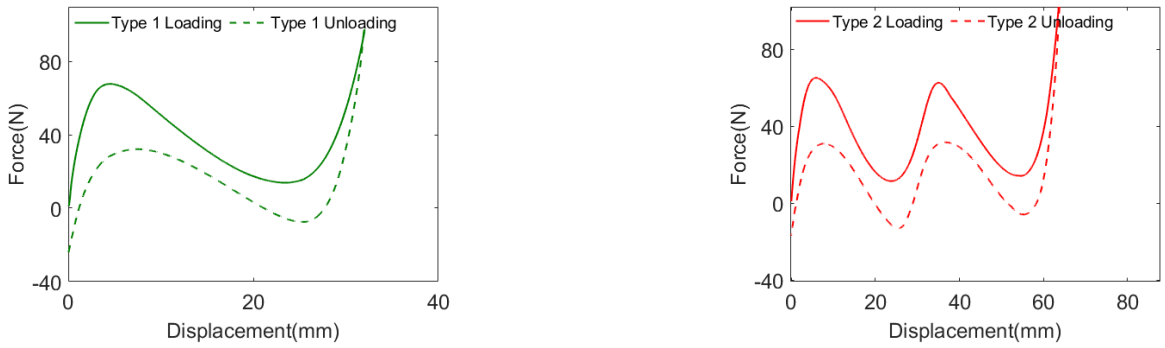

(a) (b)

Figure 4.13: Force-displacement curves for single layer of (a) Type 1 (green) (b) Type 2 layer (dark red) cylinders. Solid lines show loading (tension) and dashed shows unloading (compression) curves for Type 1 and Type 2 layers.

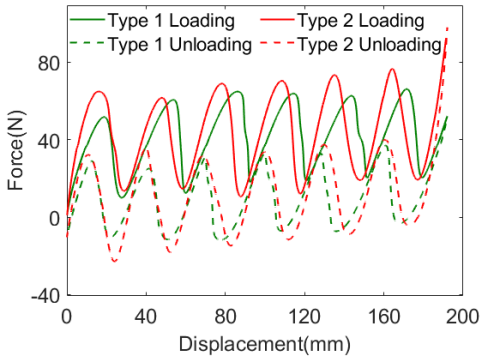

Figure 4.14: Comparison of force-displacement curves for Type 1 and Type 2 cylindrical layers with same height and radius. Type 1 consists of six layers and Type 2 consists of three layers.

state. The amount of energy absorbed was calculated by numerically integrating the force with respect to displacement. Trapezoidal integration was performed on the experimental data whose results are presented in Figure 4.15b.

The energy absorption of cylinders made of one to six Type 1 layers is plotted in Figure 4.15b. It is observed that the energy absorption in loading (tension) is always greater than in unloading (compression) irrespective of the number of layers. For instance, the energy absorbed by individual layer with 1.5 mm thickness of sinusoidal beam is 1.25 J in loading and 0.52 J in unloading. We attribute this difference to fabrication of the lattice in the collapsed state, such that this state has zero residual strain energy. When the structures were subjected to loading in tension, the finite thickness of the sinusoidal beam resisted deformation. To overcome this resistance to deformation and snap to another stable state, there was an increase in peak forces

thereby increasing the area under force - displacement curve. In the second stable state, there was residual strain stored in the sinusoidal beam. Upon unloading, the structure transitioned from a higher energy, deformed state to a lower energy collapsed state, which was attained with lower compressive forces. This resulted in lower area under the force - displacement curve and reduced energy absorption during unloading. The energy absorption results from the energy barrier that must be overcome when transitioning between stable states (Figure 1b). The energy barrier results from the high Q value of the fabricated structures. Preliminary DSC and DMA results (see Figure 4.9 and Figures 4.10 - 4.11 respectively) indicate that T_g is not within $\pm$ 20°C of room temperature. Thus, viscoelasticity is not expected to have a significant impact on energy absorption. However, as evidenced by the storage and loss modulus for a room temperature frequency sweep presented in Figure 4.10, there is a significant amount of viscous damping in the polymer at room temperature ($(G''(\omega)/G'(\omega))_{avg} = 0.164$). TPU is a block copolymer, and the data suggests that the blocks are immiscible for our material. Thus, viscous motion of soft segments (T_g less than room temperature) leads to enhanced damping during snap-through at room temperature. It is also observed that there is a steeper linear increase in energy absorption capacity in loading compared to unloading as the number of layers was increased, Figure 4.15b. When the number of layers was increased, with the dimensions of all layers being identical, every layer progresses simultaneously toward snap-through, but just one layer snapped through at a time. As an individual layer transitioned to its second stable state, the axial forces in the remaining layers was relieved. During the experiments, we observed slight separation between individual layers, which may contribute to an increase in energy absorption. As a result, energy absorption in a six layer cylinder in loading is slightly higher than $6\times$ the energy absorption for a single layer. Conversely, energy absorption during unloading in compression has a steady increasing trend because there is less influence of interfaces as the layers are compressed together, which reduces the gap between the layers.

The energy absorbed during loading and unloading can also be tuned by varying the thickness of the sinusoidal beam with all other geometric parameters constant. To demonstrate this, six Type 1 layers were printed with different sinusoidal beam thicknesses, ranging from $1.00 \leq t \leq 2.00$ mm, with an interval of 0.2 mm. The individual layers were mechanically

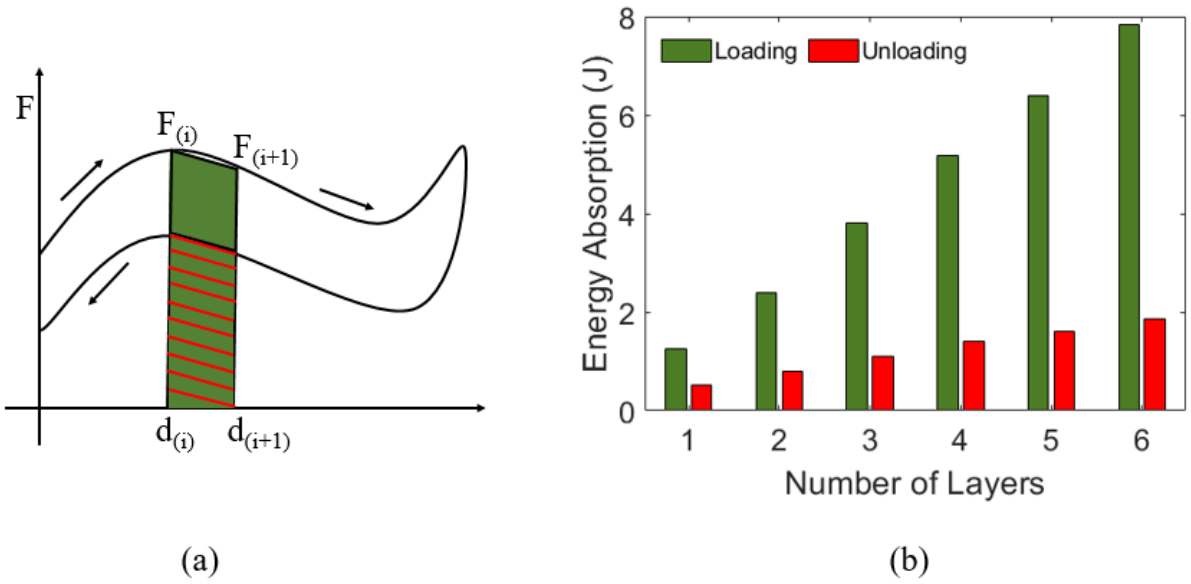

(a) (b)

Figure 4.15: (a) Schematic representation of area under cyclic loading obtained by Trapezoidal integration. The energy absorbed during loading is represented by the green area, during unloading is represented by the red area, during sequential loading and unloading. (b) Energy absorption during loading (tension) and unloading (compression) for varying number of Type 1 layers.

tested in loading (tension) and unloading (compression). The results are shown in Figure 4.16. This plot compares the energy absorption capacity of single layers, tested individually from the fully collapsed state to fully extended state and vice versa. As the beam thickness increases, so does the stiffness of the layer and the peak force required to switch between stable states. This becomes more significant for higher sinusoidal beam thicknesses, which in turn increases the energy absorption during loading (tension). For unloading (compression), there is just a slight increasing trend in energy absorption compared to loading. These characteristics of varying sinusoidal beam thickness helps to control the energy absorption in the individual layers. For instance, a single layer with t = 2.00 mm (Figure 4.16) absorbs a similar amount of energy as two Type 1 layers with a beam thickness of t = 1.5 mm (Figure 4.15).

4.4.3 Effects of sinusoidal beam thickness on snap-through sequence

Our final set of experiments considered the effects of varying the thickness (t) of the sinusoidal beam between layers to control the snapping sequence in a six-layer cylinder. Although the thickness varies from layer-to-layer, it is constant within each layer. As a demonstration, the

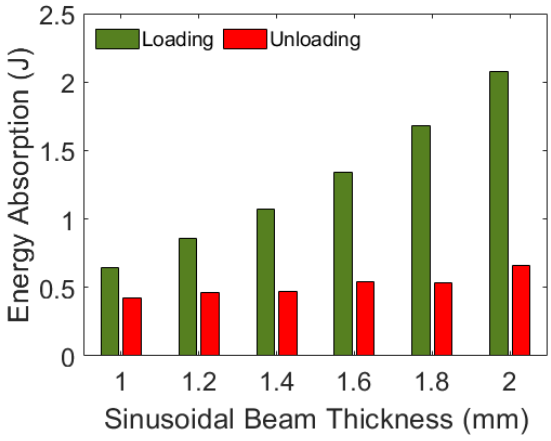

Figure 4.16: Energy absorption of individual layers during loading and unloading with thickness of sinusoidal beam ranging from 1 mm to 2 mm at an interval of 0.2 mm.

individual layers tested for Figure 4.16 were assembled in non-sequential order of beam thickness such that $t_6 > t_5 > t_3 > t_2 > t_4 > t_1$, as shown in Figure 4.17a. The subscript represents the layer number starting from the bottom. By changing the thickness of the sinusoidal beam, each layer had a different Q value (Figure 4.2b), beam stiffness, and force - displacement behavior.

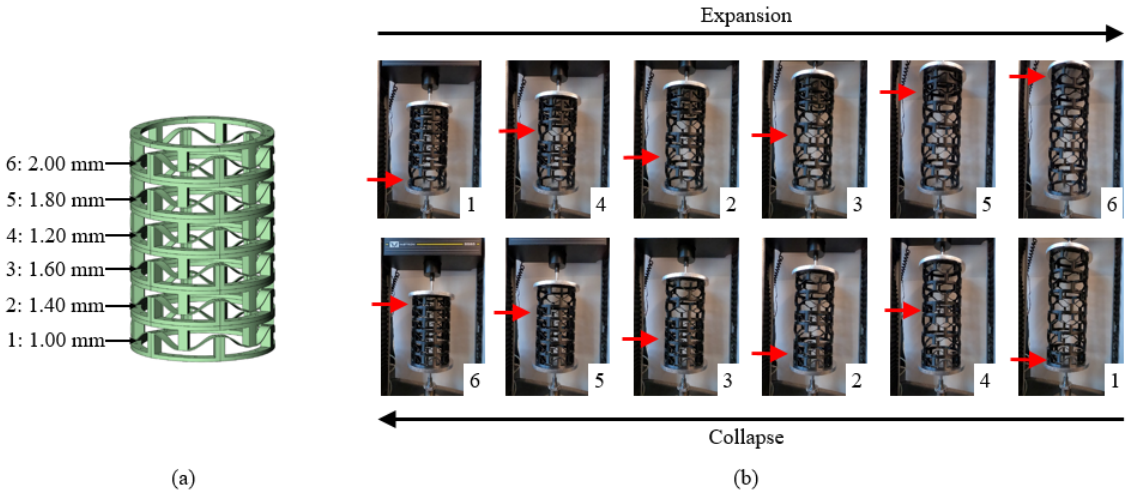

Figure 4.17: (a) Six Type 1 cylindrical layers with varying thickness were assembled in non-sequential order. (b) Snapshots showing the snapping sequence of the multistable cylinder when subjected to cyclic loading. The top row shows the loading (expansion) process in tension with a guided snapping of layers. The bottom row shows the guided collapse of layers in unloading (compression). Red arrows and white text boxes indicate which layer snaps-through in each image.

When subjected to loading (tension) and unloading (compression), the sequence of snap-through responses is shown in Figure 4.17b, wherein the red arrows and the inset white text

boxes indicate the snapping layer in each image. When load was applied starting from the undeformed (collapsed) state for the assembled cylinder, the least stiff layer, t_1, which was the first layer from bottom, snapped first. Once this layer had deformed fully, the snapping was initiated in other layers in order of increasing beam thickness. This corresponded to a higher local maximum force with increasing beam thickness. Upon unloading, the beam with lowest stiffness layer, t_1, snapped first, followed by other layers in order of increasing beam thickness. The video of the snapping is provided in the online version of this article [64].

The force - displacement curve for the loading and unloading of layers with varying thickness is shown in Figure 4.18a. The six local maximum and minimum forces in this plot correspond to the snapping of six layers of the Type 1 cylinder. The amplitude of the force - displacement curves (Figure 4.18a) during unloading (compression) appears smaller than during loading (tension), which occurs due to difference in stiffness between layers. The least stiff beam, t = 1.00 mm, had peak force values of 45.3 N (local maximum) and 4.1 N (local minimum) in loading and unloading respectively. Conversely, the stiffest beam, t = 2.00 mm, had peak force values of 145.2 N and -48 N. Between these values, the local maximum forces differ in magnitude in an increasing order, which indicates that the stiffness guides the snapping sequence.

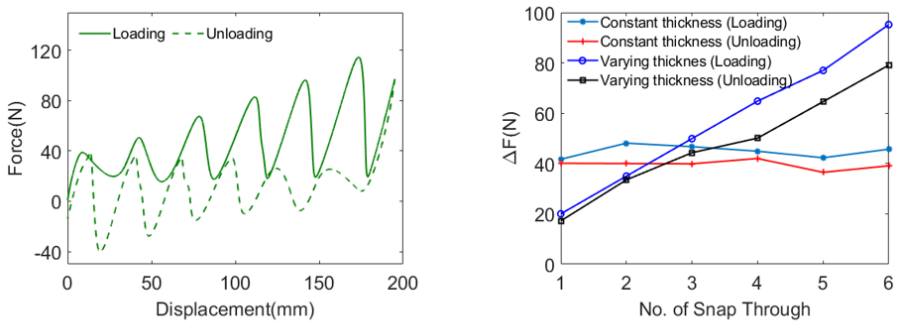

(a) (b)

Figure 4.18: (a) Force - displacement curve for the Type 1 cylinder with layers of varying thickness. The sequence of snapping occurs in order from the least thick beam layer to the thickest. (b) Magnitude of difference between local maximum and minimum forces (ΔF) along the region of negative stiffness region plotted against the number of snap-through.

Figure 4.18b shows the magnitude of the difference, ΔF, between the local maximum and minimum forces in the negative stiffness region during each snap-through for the six Type

1 layers in Figure 4.18a. It is seen that by varying beam thickness, the ΔF increases with each progressive snap-through, as expected. The value of ΔF in the negative stiffness regions during loading increases from 20 N to 95.2 N, while the snapping progresses sequentially from beam thickness of 1.00 mm to 2.00 mm. For unloading, ΔF changes from 17.2 N to 79.1 N, as the compressive snap-through progresses from the layer with t = 1.00 mm to the layer with t = 2.00 mm. For a cylinder in which each layer has matching dimensions, the magnitude for ΔF during loading and unloading (Figure 4.14) are nearly constant, as evidenced by the plot shown in Figure 4.18b. We observe in all four curves in Figure 4.18b that the difference in local maximum and minimum forces at every point during loading is greater than during unloading. This strongly supports the argument that was made earlier why energy absorption during loading (tension) is always greater than unloading (compression) due to the initial printed configuration.

4.4.4 Finite Element Analysis (FEA) Results

In this section, the FEA results are presented and discussed. Section 4.4.4.1 discusses the computational force-displacement results obtained for a single layer, uniform thickness cylinder and varying thickness cylinder to obtain controlled snapping sequence. It also compares the computational and the experimental results. Section 4.4.4.2 quantifies the energy absorption obtained computationally. It also discuses the programmability of energy absorption by varying beam thicknesses and the number of layers.

4.4.4.1 FEA Force-Displacement Results

Three Type 1 geometries were converted to finite element models. These models included a single layer with sinusoidal beam thickness of t = 1.5 mm, a six-layer cylinder in which the sinusoidal beam thickness in each layer was t = 1.5 mm, and a six-layer cylinder matching the configuration shown in Figure 4.17a. The six-layer cylinders were modeled as a single piece, rather than having discontinuities at the layer interfaces to evaluate any differences between a single piece structure versus the assembled experimental specimens. As shown in Figure 4.21, it is observed that the stresses in the computational models are localized to the sinusoidal

beams, which experience significant deformation throughout the extension and compression cycle. Additionally, it is observed that a residual stress is present after snapping through from the initial state to the second stable state. Images showing the deformed computational models can be found in Figure 4.19 and Figure 4.20. For the six-layer cylinder with uniform beam thickness, it was observed that the snap-through response occurs first in the central layers of the cylinder, with the top and bottom layers snapping through last. For the six-layer cylinder with varying beam thickness, it is seen that beam thickness determines the snap-through sequence during loading, and the order matches the experimental results (i.e., the snapping sequence is 1-4-2-3-5-6). However, during unloading, the snapping sequence progresses from bottom to top and is affected by the peak forces required to initiate snap-through and interactions between layers as discussed later.

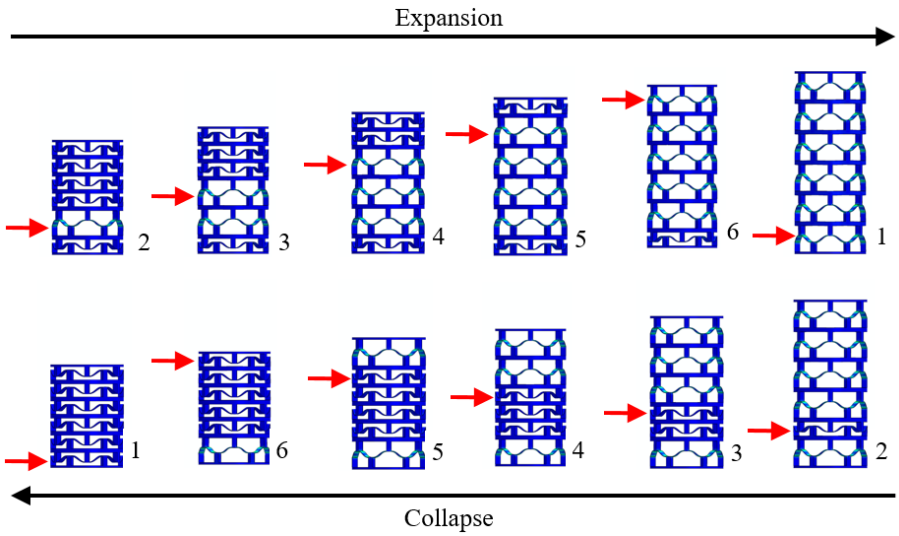

Figure 4.19: Computational images for random snapping sequence when the thickness of sinusoidal beam is uniform (1.5 mm).

Force displacement results from the finite element analysis of a single layer are shown in Figure 4.22. The FEA results (solid lines) are overlaid with the experimental results (dashed lines). It is seen that the computational model slightly overpredicts the peak force required to initiate snap-through. This mismatch results from an overshoot of the force as snap-through begins. Between the local maximum and minimum forces, the loading and unloading curves nearly coincide, which does not agree with the experimental results. This disagreement may result from the material model.

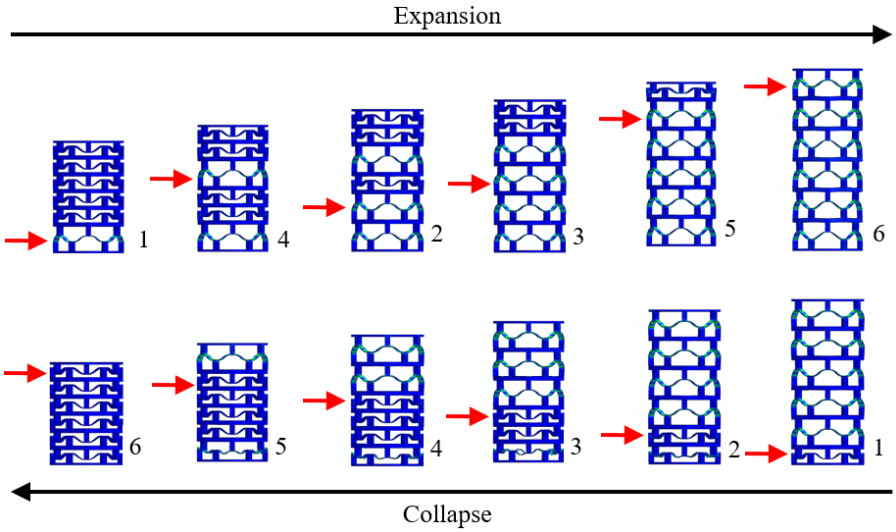

Figure 4.20: Computational images for controlled snapping sequence when the thickness of sinusoidal beam varies from 1 mm to 2 mm.

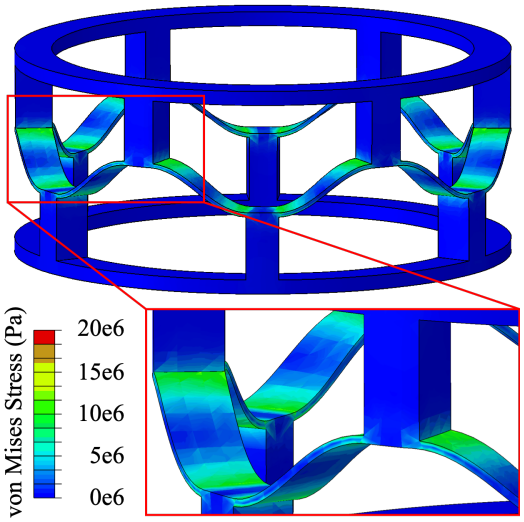

Figure 4.21: Example from FEA of a deformed Type 1 layer. Contours are for von Mises stress with units in Pa. The inset shows a closeup of the stress contours on the deformed structure. Even though the structure is in its second stable state, the residual stress persists.

Results from the finite element analysis of six Type 1 layers having a uniform sinusoidal beam thickness of 1.5 mm are shown in Figure 4.23 (snap-through sequence shown in Figure 4.19). The FEA results (solid lines) are overlaid with the experimental results (dashed lines). It is seen that the model again slightly overpredicts the maximum and minimum forces during both loading and unloading. During loading, the strain for snap-through gradually shifts towards the left relative to the experimental results. During unloading, the strain for each snap-through agrees well with the experimental results. It is also observed that the loading and

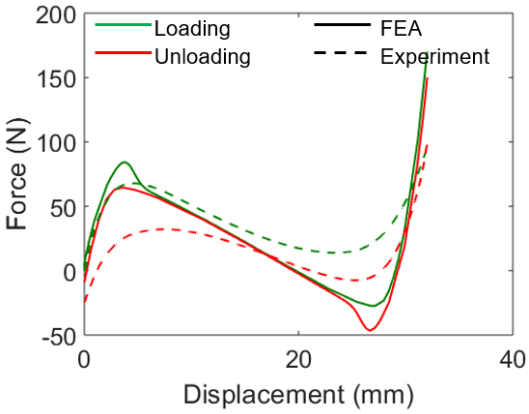

Figure 4.22: FEA results for a single, Type 1 layer with t = 1.5 mm. Computational results (solid lines) are overlaid with experimental results (dashed lines). The green lines are for the loading portion and the red lines are for the unloading portion.

unloading curves do not coincide in the negative stiffness region as they did for the single layer model.

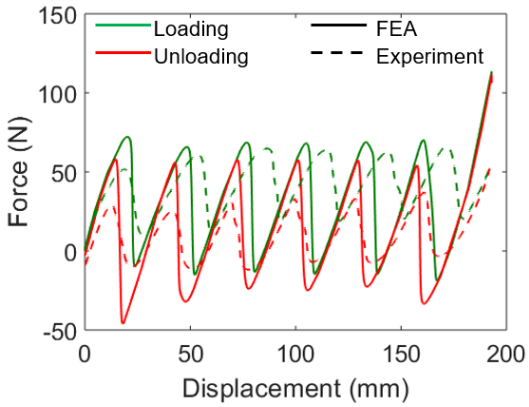

Figure 4.23: FEA results for a six-layer, Type 1 cylinder with t = 1.5 mm. Computational results (solid lines) are overlaid with experimental results (dashed lines). The green lines are for the loading portion and the red lines are for the unloading portion.

Results from the finite element analysis of six Type 1 layers wherein the sinusoidal beam thickness varies between layers are shown in Figure 4.24 (snap-through sequence shown in Figure 4.20). The configuration for this model matches the configuration in Figure 4.17a. The FEA results (solid lines) are overlaid with the experimental results (dashed lines). In this analysis, it was observed that the snap-through sequence during loading agreed with the experimental result. However, during unloading, the snap-through sequence was 1-2-3-4-5-6. Close observation of the computational model during these segments indicates that as layers with $t \geq 1.2$ mm collapse, their strain is redistributed throughout the cylinder. Because the

force required to initiate an opening snap-through of the layer with $t = 1.0$ mm is similar to the contracting force of the other layers, the former tends to re-open as the other layers close. Once again, the computational model tends to overpredict the experimental force-displacement results, but the overall trends agree well. Unexpected spikes during the second through sixth snap-throughs are observed during the unloading portion in Figure 4.24. Upon comparison, these spikes coincide with jogs in the experimental results, which have been observed by other researchers [95].

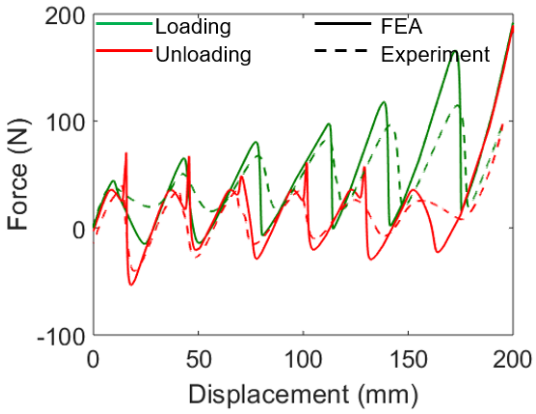

Figure 4.24: FEA results for a six-layer, Type 1 cylinder with varying beam thickness. Computational results (solid lines) are overlaid with experimental results (dashed lines). The green lines are for the loading portion and the red lines are for the unloading portion.

4.4.4.2 FEA Energy Absorption Results

Results from the finite element analysis were used to calculate energy aborption for cylinders with a varying number of layers having $t = 1.5$ mm, as shown in Figure 4.25a, and for individual layers with varying thicknesses from 1 mm to 2 mm, as shown in Figure 4.25b. The comparison of the energy absorption during loading and unloading indicates the energy absorption in loading is always greater than the energy absorption in unloading, which has also been discussed earlier in experimental section. The energy absorption in loading is in good agreement with the computational results. However, the computational results slightly overpredicts the compressive forces, resulting in higher value for energy absorption during unloading as compared to experimental results.

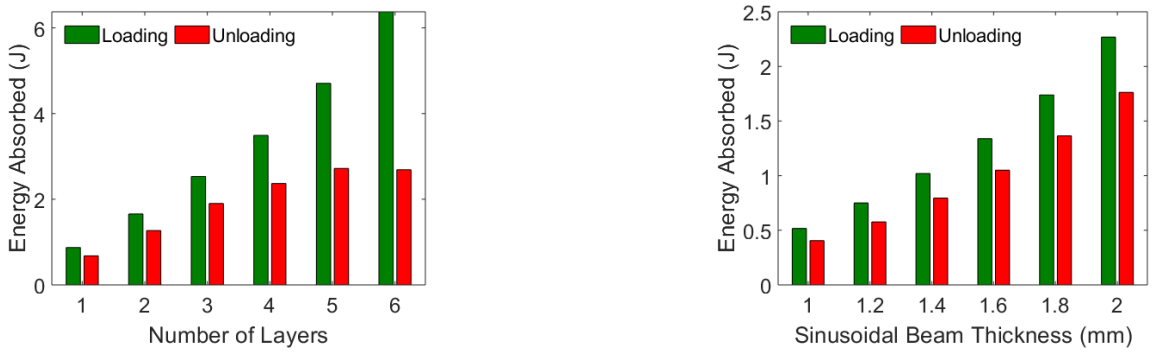

(a) (b)

Figure 4.25: Computational results for energy absorption during loading and unloading when (a) varying the number of layers with t = 1.5 mm and (b) individual layers with thickness of sinusoidal beam ranging from 1 mm to 2 mm at an interval of 0.2 mm.

4.5 Conclusion

Herein, we investigated multistable cylindrical layers consisting of bistable unit cells. Bistable cylindrical layers were fabricated using FDM with TPU filament. This investigation contributes insight into the behavior of bistable unit cells incorporated into the walls of cylindrical structures. We studied the mechanical behavior of the cylinders in both loading (tension) and unloading (compression) and quantify the energy absorption during deformation. Additionally, we investigated techniques to tailor the energy absorption and snapping sequence of multistable cylinders. Comparisons were made between analytical, experimental, and computational results.

In the experimental studies, force - displacement curves indicated that the loading (tension) and unloading (compression) curves do not coincide. Clear snap-through responses were seen in experimental and computational results for the cylinders. Peak forces in the experimental results agreed well with analytical models for planar bistable structures. The mechanical responses of Type 1 (single snap-through element) and Type 2 (double snap-through element, mirrored Type 1 unit cells) cylinders were observed to be similar with a slight discrepancy attributed to manufacturing variations and the interface between layers. This suggests that multiple Type 1 layers could be used to estimate the behavior of Type 2 structures. The force-displacement curves enclose an area, which means that the bistable cylindrical layers are capable of energy absorption. The energy absorption behavior is attributed to viscous energy

dissipation of the soft segments of the TPU block copolymer used to fabricate the cylinders. The number of layers and thickness of the sinusoidal beam in each layer were varied to study the mechanical response and guided snapping sequence in Type 1 and Type 2 multistable cylinders.

For a multistable cylinder consisting of bistable layers, energy absorption capacity in loading (tension) was always greater than in unloading (compression). This difference was more significant with an increase in the number of layers and corresponded to the energy dissipation capacity of these structures. For instance, with a sinusoidal beam thickness of t = 1.5 mm, the energy absorption for a single layer was 1.25 J during loading (tension) and 0.52 J during unloading (compression), and the energy absorption for six layers was 7.84 J during loading and 1.86 J during unloading. Energy absorption capacity can also be tuned by changing the thickness of the sinusoidal beam in each layer with all other parameters being constant. For a multilayer cylinder (i.e., two or more than two Type 1 layers or one or more Type 2 layers), the transition of snap-through from one layer to another was random for the same geometric parameters. The layer with the minimum peak force snaps-through first to the second stable configuration and then the snap-through occurs in the rest of the layers as the displacement progresses. The thickness of the sinusoidal beam in each layer, which changes the geometric parameter Q of the layer, can be varied to guide the snapping sequence from one layer to another and tailor the energy absorption. It was demonstrated what a layer with a t = 1.0 mm thick sinusoidal beam has an energy absorption of 0.65 J during loading and 0.42 J during unloading, and a layer with a t = 2.0 mm thick sinusoidal beam has an energy absorption of 2.08 J during loading and 0.66 J during unloading.

Results from computational models agreed well with experimental results. The snap-through behavior of multistable cylinders was modeled using a three-dimensional finite element analysis using a dynamic implicit algorithm and a linear elastic material model with stiffness proportional damping. FEA predictions of energy absorption agreed well with experimental results in loading, but overpredicted energy absorption in unloading. In the FEA during unloading, it was observed that contraction forces of stiffer layers had a tendency to reopen the least stiff layer, resulting in irregularities in the force - displacement results that are observed

in the experimental results. The computational model also offered a comparison of the difference in mechanical behavior of the assembled experimental samples and a computationally modeled, one-piece cylinder. The model indicated that assembling the experimental specimen from multiple layers has a negligible effect on the bistable behavior. The determination of programmable energy absorption and guided snapping sequence in multistable cylindrical layers is desirable in several applications such as control of propagation of elastic waves [114–117] and deployable morphing structures [118–123]. The findings can have applications beyond cylindrical structures where the multistable structure must respond to tensile or compressive loads with programmable energy absorption.

Chapter 5

Summary and Future Work

5.1 Summary

In this thesis, negative Poisson's ratio and bistable mechanical metamaterials were presented and analyzed. These metamaterials were additively manufactured using FDM. Combination of mismatched repeat units in auxetic lattice structures was analyzed which led to adjustable stiffness in those structures. Similarly, planar and cylindrical bistable metamaterials were studied to evaluate their mechanical behavior. Variation of thickness of sinusoidal beams was implemented to control the snapping sequence of the cylindrical layers whereas variation of thickness of sinusoidal beams and varying the number of layers techniques were used to program the energy absorption of bistable structures. Here is a brief chapterwise summary:

Chapter 1 laid the background of lattice structures and how humans have been trying to imitate the natural lattice structures into various applications for improved properties such as energy absorption, shock absorption and to reduce weight while maintaining the structural integrity. The chapter then discussed about modern technologies to manufacture these lattices. AM techniques like Fused Deposition Modeling (FDM), which uses thermoplastic filaments, are being used to manufacture the lattice structures because of their ability to manufacture complex geometries. This chapter was then followed by the discussion on mechanical metamaterials which are lattice structures with unique properties such as negative Poisson's ratio and bistability. Then, this chapter discussed the analytical part of bistable unit cell highlighting the key parameter Q (height to thickness ratio) in designing the bistable structures, which determines the bistability of the structures. This chapter also discussed the recent developments of

mechanical metamaterials. This chapter further provided information on practical use cases of these structures in the field.

Chapter 2 highlighted auxetic metamaterials. This chapter focused on design, fabrication and testing of various combination of traditional honeycomb and re-entrant structures. Honeycomb and re-entrant honeycomb unit cells were used to tessellate for various combinations in a 3*3 array. The structures were 3D printed using PLA in a Makerbot Replicator+. Quasi static tests were performed on all of the lattice structures at room temperature at strain rate of 4 mm/min. Force-displacement behavior were fairly linear in X-direction and non-linear response in Y-direction. It was because of the fact that while loading in X direction, the ligaments aligned to testing direction whereas while loading in Y direction, the ligaments initially rotated followed by tension in ligaments. The study showed that the stiffness of the system can be tuned by adding defects and changing the loading direction of the system. The graphs showed promising results to tune the stiffness those structures.

Chapter 3 discussed the bistable planar structures. This chapter presented design and fabrication of additively manufactured bistable planar structures using TPU. The structures were printed in two different configurations: collapsed and expanded. They were fabricated in different arrangements of rows and columns from 1*1 to 3*3. It was observed that the bistable structures had a non-linear mechanical response. The force-displacement curves showed clear local maximum and minimum points indicating the snap-through. All the lattice structures exhibited clear bistable behavior except for a column of 3*1 because of the rotation of the repeat units.

Chapter 4 discussed recent developments in the field of multistable structures. This chapter progressed from the bistable planar structure in Chapter 3 to bistable cylindrical structure. This chapter discussed the mechanical behavior of curved bistable beam. This chapter discussed the effects of changing the geometric parameter Q on the mechanical behavior. It was discussed that bistability is achieved at $Q = 2.31$ and beyond. The structure is monostable when the value is less than 2.31. Type 1 and Type 2 cylindrical structures were fabricated using flexible filament (TPU) with the same value of Q. Sequential tension and compression tests were performed at room temperature on Type 1 and Type 2 layers. It was found that the both Type 1 and

Type 2 exhibit the same mechanical behavior and the snapping forces were in good agreement with the analytical model. Further, the thickness of sinusoidal beams were varied between the layers to guide the snapping sequence. It was found that the layer with the least thickness snaps first followed by increasing thickness. Energy absorption was also computed for varying number of layers and varying thickness. This chapter concluded that energy absorption of these structures can be tuned with varying the number of layers and thickness of sinusoidal beam. The energy absorption in loading was always greater than during unloading for the printed configuration. The effects of variation of number of layers and thickness were studied computationally. Computational results were in good agreement with the experimental results for energy absorption and snapping sequence.

Finally, Chapter 5 summarizes the results of this thesis, complete with details about their furthered and continued impact as well as a discussion about their contributions to the existing fields of knowledge. A discussion of further work using this thesis as a starting point is included.

5.2 Future Work

Mechanical metamaterials being a useful and vast research area, has numerous aspects to be investigated. Below I present some of the ideas that I think could be done in the field of mechanical metamaterials that I presented in this thesis.

For the lattice structures presented in Chapter 2:

- It could be interesting to consider the effect of temperature on stiffness while testing the lattice structures. The test could run for a temperature range of room temperature to temperature slightly above the glass transition of the material used for the fabrication of structures. For performing this kind of experiment, a thermal chamber could be designed using material like polycarbonate and heating elements that goes around the testing region of tensile testing instrument, refer Figure 5.1. This kind of test is called thermo-mechanical test where the tensile test is carried out simultaneously with the application of heat. The temperature inside the heating chamber could be adjusted using the

heating rods and sensors within the chamber. The challenge would be to maintain constant temperature all around the chamber for a particular test at particular temperature. For this, elements could be used inside the chamber with a fan that could circulate the heat all around the chamber. The fan should work pretty well, upto the desired maximum temperature, that is, fan that works till 100 °C might work when PLA is used.

- The similar lattice structures could be printed with greater extrusion height and without the custom test fixture arrangement. The structures then could be investigated for impact test and crushing load. This could help to identify the most suitable arrangement of defects to tune the impact resistance of these structures. The structures might find applications in areas where the crushing load and behavior plays an important role.

- For the tests mentioned in above two bullet points, it could be worth performing the computational modeling. The computational results then could be compared to the experimental results. The boundary conditions for the computational modeling should represent the actual experimental setup. The parameters such as Young's Modulus, Poisson's ratio, material density should be computed from the results obtained the test of a dog-bone sample using ASTM standards. For performing computation involving thermomechanical test, input parameters can be used using DMA which characterizes a material's properties as a function of temperature, time, frequency, stress, or a combination of these parameters.

For the bistable structures presented in Chapter 3 and Chapter 4:

- It could be worth analyzing the energy absorption of the structures in two different configuration. It means the bistable structures could be designed and fabricated in collapsed and extended configuration with same Q value as shown in Figure 5.2. Various arrangement of unit cell along rows and columns could be fabricated as in Chapter 3. Test procedure similar to Chapter 3 could be applied for each individual structure. The test fixture could be similar to test fixture in Chapter 4, but instead of circular plate, flat plate could be used with appropriate screw fixture arrangement. The energy absorption then could be computed for these two different structures and a conclusion could be drawn

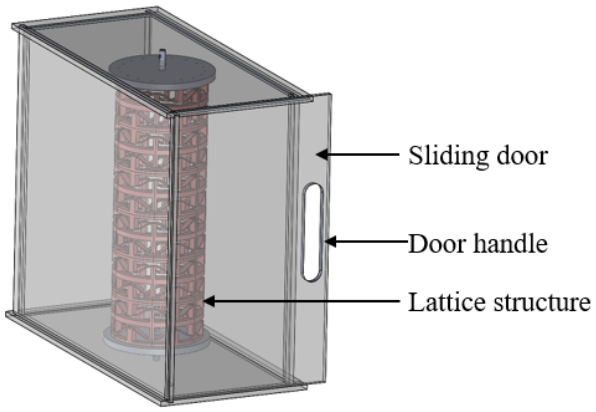

Figure 5.1: Thermal chamber that could be made with six faces of polycarbonates with a sliding door mechanism in front to insert the sample. Top and bottom faces could be provided with openings to connect the sample with the testing machine

whether or not the printing configuration has effect on energy absorption for these kind of metamaterials. This could be an important conclusion since all lattice metamaterials are fabricated using AM technique.

- Multistable structures consisting of bistable unit cells have a potential applications in morphing structures especially in aerospace industry. So, it could be worth studying the eccentric testing of the cylindrical multistable structures under tension and compression. The major challenge would be to carry out the test. It would require major investigation on customizing the testing fixture and also on performing the test with ASTM requirements. One potential way to customize the test fixture could be modify the test fixture that was used for cylindrical layers in Chapter 4. For this, a hole to fit top rod that connects the plate to Instron could be made approximately 3 mm away from the center. The hole could be made slanted at an angle of 10° with the vertical, refer Figure 5.3. Then the structure could be tested in tension and compression and its mechanical behavior, snapping mechanism and energy absorption could be analyzed. The results might not show clear snap-through since once side of the structure would always try to remain in compression. The result might show greater reason of hysteresis loop which could be analyzed based on the snapping pattern. The results might be useful for design and analysis of these structures when used as morphing structures.

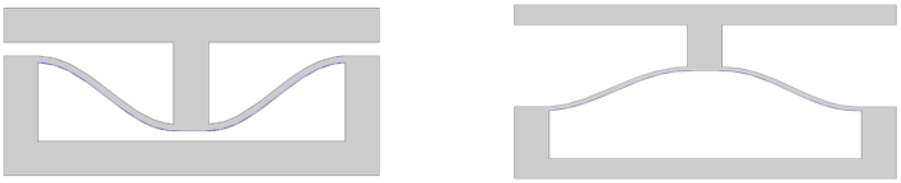

(a) (b)

Figure 5.2: Bistable unit cell in (a) collapsed state (b) expanded state

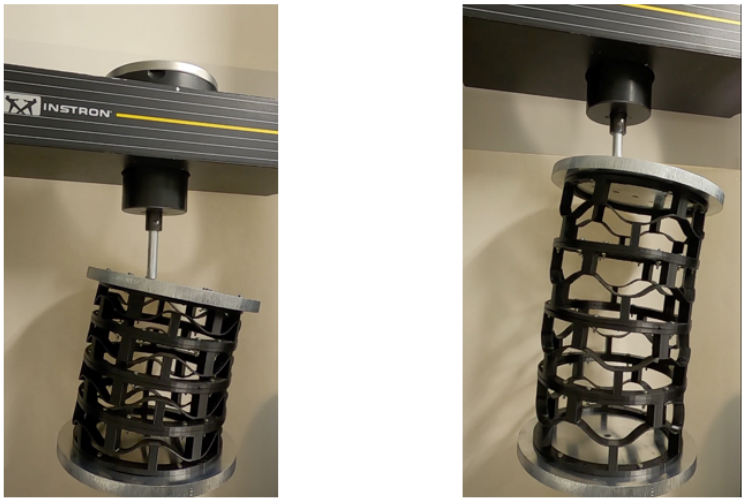

(a) (b)

Figure 5.3: Eccentric test fixture arrangement of multistable cylindrical structure in (a) collapsed state (b) expanded state

References

[1] T. Maconachie, M. Leary, B. Lozanovski, X. Zhang, M. Qian, O. Faruque, and M. Brandt, "SLM lattice structures: Properties, performance, applications and challenges," *Materials and Design*, vol. 183, p. 108137, 2019.

[2] J. H. Lee, J. P. Singer, and E. L. Thomas, "Micro-/nanostructured mechanical metamaterials," *Advanced Materials*, vol. 24, no. 36, pp. 4782–4810, 2012.

[3] D. Smith, D. Vier, T. Koschny, and C. Soukoulis, "Electromagnetic parameter retrieval from inhomogeneous metamaterials," *Physical review E*, vol. 71, no. 3, p. 036617, 2005.

[4] J. Mei, G. Ma, M. Yang, Z. Yang, W. Wen, and P. Sheng, "Dark acoustic metamaterials as super absorbers for low-frequency sound," *Nature Communications*, vol. 3, 2012.

[5] S. Vignolini, N. A. Yufa, P. S. Cunha, S. Guldin, I. Rushkin, M. Stefik, K. Hur, U. Wiesner, J. J. Baumberg, and U. Steiner, "A 3D optical metamaterial made by self-assembly," *Advanced Materials*, vol. 24, no. 10, pp. 23–27, 2012.

[6] L. Wu, B. Li, and J. Zhou, "Isotropic negative thermal expansion metamaterials," *ACS applied materials & interfaces*, vol. 8, no. 27, pp. 17721–17727, 2016.

[7] W. Wu, W. Hu, G. Qian, H. Liao, X. Xu, and F. Berto, "Mechanical design and multifunctional applications of chiral mechanical metamaterials: A review," *Materials & Design*, vol. 180, p. 107950, 2019.

[8] Z. G. Nicolaou and A. E. Motter, "Mechanical metamaterials with negative compressibility transitions," *Nature Materials*, vol. 11, no. 7, pp. 608–613, 2012.

[9] T. A. Schaedler and W. B. Carter, "Architected Cellular Materials," *Annual Review of Materials Research*, vol. 46, pp. 187–210, 2016.

[10] J. H. Lee, J. P. Singer, and E. L. Thomas, "Micro-/nanostructured mechanical metamaterials," *Advanced Materials*, vol. 24, no. 36, pp. 4782–4810, 2012.

[11] C. S. Ha, R. S. Lakes, and M. E. Plesha, "Design, fabrication, and analysis of lattice exhibiting energy absorption via snap-through behavior," *Materials and Design*, vol. 141, pp. 426–437, 2018.

[12] E. B. Duoss, T. H. Weisgraber, K. Hearon, C. Zhu, W. Small IV, T. R. Metz, J. J. Vericella, H. D. Barth, J. D. Kuntz, R. S. Maxwell, C. M. Spadaccini, and T. S. Wilson, "Three-dimensional printing of elastomeric, cellular architectures with negative stiffness," *Advanced Functional Materials*, vol. 24, no. 31, pp. 4905–4913, 2014.

[13] J.-H. Lee, L. Wang, S. Kooi, M. C. Boyce, and E. L. Thomas, "Enhanced energy dissipation in periodic epoxy nanoframes," *Nano letters*, vol. 10, no. 7, pp. 2592–2597, 2010.

[14] B. Florijn, C. Coulais, and M. Van Hecke, "Programmable mechanical metamaterials," *Physical Review Letters*, vol. 113, no. 17, pp. 1–5, 2014.

[15] A. G. Evans, M. Y. He, V. S. Deshpande, J. W. Hutchinson, A. J. Jacobsen, and W. B. Carter, "Concepts for enhanced energy absorption using hollow micro-lattices," *International Journal of Impact Engineering*, vol. 37, no. 9, pp. 947–959, 2010.

[16] D. M. Correa, T. Klatt, S. Cortes, M. Haberman, D. Kovar, and C. Seepersad, "Negative stiffness honeycombs for recoverable shock isolation," *Rapid Prototyping Journal*, vol. 21, no. 2, pp. 193–200, 2015.

[17] B. A. Fulcher, D. W. Shahan, M. R. Haberman, C. C. Seepersad, and P. S. Wilson, "Analytical and experimental investigation of buckled beams as negative stiffness elements for passive vibration and shock isolation systems," *Journal of Vibration and Acoustics, Transactions of the ASME*, vol. 136, no. 3, pp. 1–12, 2014.

[18] L. Kashdan, C. C. Seepersad, M. Haberman, and P. S. Wilson, "Design, fabrication, and evaluation of negative stiffness elements using SLS," *Rapid Prototyping Journal*, vol. 18, no. 3, pp. 194–200, 2012.

[19] T. Frenzel, C. Findeisen, M. Kadic, P. Gumbsch, and M. Wegener, "Tailored Buckling Microlattices as Reusable Light-Weight Shock Absorbers," *Advanced Materials*, vol. 28, no. 28, pp. 5865–5870, 2016.

[20] J. U. Surjadi, L. Gao, H. Du, X. Li, X. Xiong, N. X. Fang, and Y. Lu, "Mechanical Metamaterials and Their Engineering Applications," *Advanced Engineering Materials*, vol. 21, no. 3, pp. 1–37, 2019.

[21] Dalgaç, F. Karadağ, M. Bakır, O. Akgöl, E. Ünal, and M. Karaaslan, "Chiral metamaterial-based sensor applications to determine quality of car lubrication oil," *Transactions of the Institute of Measurement and Control*, vol. 43, no. 7, pp. 1640–1649, 2020.

[22] S. Dalgac, V. Akdogan, S. Kiris, A. Incesu, O. Akgol, E. Unal, M. T. Basar, and M. Karaaslan, "Investigation of methanol contaminated local spirit using metamaterial based transmission line sensor," *Measurement*, vol. 178, no. October 2020, p. 109360, 2021.

[23] Y. I. Abdulkarim, F. F. Muhammadsharif, M. Bakır, H. N. Awl, M. Karaaslan, L. Deng, and S. Huang, "Hypersensitized metamaterials based on a corona-shaped resonator for efficient detection of glucose," *Applied Sciences (Switzerland)*, vol. 11, no. 1, pp. 1–19, 2021.

[24] S. Kacin, M. Ozturk, U. K. Sevim, B. A. Mert, Z. Ozer, O. Akgol, E. Unal, and M. Karaaslan, "Seismic metamaterials for low-frequency mechanical wave attenuation," *Natural Hazards*, no. 0123456789, 2021.

[25] J. Qiu, J. H. Lang, and A. H. Slocum, "A curved-beam bistable mechanism," *Journal of Microelectromechanical Systems*, vol. 13, no. 2, pp. 137–146, 2004.

[26] D. Restrepo, N. D. Mankame, and P. D. Zavattieri, "Phase transforming cellular materials," *Extreme Mechanics Letters*, vol. 4, pp. 52–60, 2015.

[27] T. R. Giri and R. Mailen, "Two-dimensional mechanical metamaterials with adjustable stiffness and damping," no. May, p. 37, 2020.

[28] S. Babaee, J. Shim, J. C. Weaver, E. R. Chen, N. Patel, and K. Bertoldi, "3D soft metamaterials with negative poisson's ratio," *Advanced Materials*, vol. 25, no. 36, pp. 5044–5049, 2013.

[29] R. Lakes, "Foam structures with a negative poisson's ratio," *Science*, vol. 235, pp. 1038–1041, 1987.

[30] R. Gatt and J. N. Grima, "Negative compressibility," *physica status solidi (RRL)–Rapid Research Letters*, vol. 2, no. 5, pp. 236–238, 2008.

[31] X. Zheng, H. Lee, T. H. Weisgraber, M. Shusteff, J. DeOtte, E. B. Duoss, J. D. Kuntz, M. M. Biener, Q. Ge, J. A. Jackson, S. O. Kucheyev, N. X. Fang, and C. M. Spadaccini, "Ultralight, ultrastiff mechanical metamaterials," *Science*, vol. 344, no. 6190, pp. 1373–1377, 2014.

[32] W. Yang, Z. M. Li, W. Shi, B. H. Xie, and M. B. Yang, "On auxetic materials," *Journal of Materials Science*, vol. 39, no. 10, pp. 3269–3279, 2004.

[33] H. M. Kolken and A. A. Zadpoor, "Auxetic mechanical metamaterials," *RSC Advances*, vol. 7, no. 9, pp. 5111–5129, 2017.

[34] J. I. Lipton, R. MacCurdy, Z. Manchester, L. Chin, D. Cellucci, and D. Rus, "Handedness in shearing auxetics creates rigid and compliant structures," *Science*, vol. 360, no. 6389, pp. 632–635, 2018.

[35] R. Gatt, L. Mizzi, J. I. Azzopardi, K. M. Azzopardi, D. Attard, A. Casha, J. Briffa, and J. N. Grima, "Hierarchical Auxetic Mechanical Metamaterials," *Scientific Reports*, vol. 5, pp. 1–6, 2015.

[36] K. Bertoldi, P. M. Reis, S. Willshaw, and T. Mullin, "Negative poisson's ratio behavior induced by an elastic instability," *Advanced Materials*, vol. 22, no. 3, pp. 361–366, 2010.

[37] J. Lee, J. B. Choi, and K. Choi, "Application of homogenization FEM analysis to regular and re-entrant honeycomb structures," *Journal of Materials Science*, vol. 31, no. 15, pp. 4105–4110, 1996.

[38] M. Shokri Rad, Y. Prawoto, and Z. Ahmad, "Analytical solution and finite element approach to the 3D re-entrant structures of auxetic materials," *Mechanics of Materials*, vol. 74, pp. 76–87, 2014.

[39] L. Yang, O. Harrysson, H. West, and D. Cormier, "Modeling of uniaxial compression in a 3D periodic re-entrant lattice structure," *Journal of Materials Science*, vol. 48, no. 4, pp. 1413–1422, 2013.

[40] D. Prall and R. Lakes, "Properties of chiral honeycombe with Poisson's ratio of -1," *Int. J. Mech. Sci*, vol. 39, no. 3, 1997.

[41] A. Alderson, K. L. Alderson, D. Attard, K. E. Evans, R. Gatt, J. N. Grima, W. Miller, N. Ravirala, C. W. Smith, and K. Zied, "Elastic constants of 3-, 4- and 6-connected chiral and anti-chiral honeycombs subject to uniaxial in-plane loading," *Composites Science and Technology*, vol. 70, no. 7, pp. 1042–1048, 2010.

[42] G. Carta, M. Brun, and A. Baldi, "Design of a porous material with isotropic negative Poisson's ratio," *Mechanics of Materials*, vol. 97, pp. 67–75, 2016.

[43] D. Attard and J. N. Grima, "Auxetic behaviour from rotating rhombi," *Physica Status Solidi (B) Basic Research*, vol. 245, no. 11, pp. 2395–2404, 2008.

[44] G. Imbalzano, P. Tran, T. D. Ngo, and P. V. Lee, "A numerical study of auxetic composite panels under blast loadings," *Composite Structures*, vol. 135, pp. 339–352, 2016.

[45] K. E. Evans and A. Alderson, "Auxetic materials: Functional materials and structures from lateral thinking!," *Advanced Materials*, vol. 12, no. 9, pp. 617–628, 2000.

[46] R. S. Lakes and K. Elms, "Indentability of Conventional and Negative Poisson's Ratio Foams," *Journal of Composite Materials*, vol. 27, no. 12, pp. 1193–1202, 1993.

[47] A. Bezazi, W. Boukharouba, and F. Scarpa, "Mechanical properties of auxetic carbon/epoxy composites: Static and cyclic fatigue behaviour," *Physica Status Solidi (B) Basic Research*, vol. 246, no. 9, pp. 2102–2110, 2009.

[48] R. Critchley, I. Corni, J. A. Wharton, F. C. Walsh, R. J. Wood, and K. R. Stokes, "A review of the manufacture, mechanical properties and potential applications of auxetic foams," *Physica Status Solidi (B) Basic Research*, vol. 250, no. 10, pp. 1963–1982, 2013.

[49] L. Foster, P. Peketi, T. Allen, T. Senior, O. Duncan, and A. Alderson, "Application of auxetic foam in sports helmets," *Applied Sciences (Switzerland)*, vol. 8, no. 3, pp. 1–12, 2018.

[50] K. Kuribayashi, K. Tsuchiya, Z. You, D. Tomus, M. Umemoto, T. Ito, and M. Sasaki, "Self-deployable origami stent grafts as a biomedical application of Ni-rich TiNi shape memory alloy foil," *Materials Science and Engineering A*, vol. 419, no. 1-2, pp. 131–137, 2006.

[51] J. N. Grima, L. Oliveri, D. Attard, B. Ellul, R. Gatt, G. Cicala, and G. Recca, "Hexagonal honeycombs with zero Poisson's ratios and enhanced stiffness," *Advanced Engineering Materials*, vol. 12, no. 9, pp. 855–862, 2010.

[52] K. E. Evans, "Auxetic polymers: a new range of materials," *Endeavour*, vol. 15, no. 4, pp. 170–174, 1991.

[53] W. Wu, W. Hu, G. Qian, H. Liao, X. Xu, and F. Berto, "Mechanical design and multifunctional applications of chiral mechanical metamaterials: A review," *Materials and Design*, vol. 180, no. June, p. 107950, 2019.

[54] J. Huang, Q. Zhang, F. Scarpa, Y. Liu, and J. Leng, "In-plane elasticity of a novel auxetic honeycomb design," *Composites Part B: Engineering*, vol. 110, pp. 72–82, 2017.

[55] J. N. GRIMA, A. ALDERSON, and K. E. EVANS, "Negative Poisson'S Ratios From Rotating Rectangles," *Computational Methods in Science and Technology*, vol. 10, no. 2, pp. 137–145, 2004.

[56] V. Carneiro, J. Meireles, and H. Puga, "Auxetic materials—a review," *Materials Science-Poland*, vol. 31, no. 4, pp. 561–571, 2013.

[57] J. W. Steeds, "The Royal Society is collaborating with JSTOR to digitize, preserve, and extend access to Proceedings of the Royal Society of London. Series A, Mathematical and Physical Sciences. ® www.jstor.org," *Proceedings Of The Royal Society Of London Series A-Mathematical And Physical Sciences*, vol. 292, no. 1430, pp. 343–373, 1966.

[58] A. Ingrole, A. Hao, and R. Liang, "Design and modeling of auxetic and hybrid honeycomb structures for in-plane property enhancement," *Materials and Design*, vol. 117, pp. 72–83, 2017.

[59] A. Alderson, K. L. Alderson, G. Chirima, N. Ravirala, and K. M. Zied, "The in-plane linear elastic constants and out-of-plane bending of 3-coordinated ligament and cylinder-ligament honeycombs," *Composites Science and Technology*, vol. 70, no. 7, pp. 1034–1041, 2010.

[60] J. Zhang, G. Lu, and Z. You, "Large deformation and energy absorption of additively manufactured auxetic materials and structures: A review," *Composites Part B: Engineering*, vol. 201, no. August, p. 108340, 2020.

[61] J. Huang, Q. Zhang, F. Scarpa, Y. Liu, and J. Leng, "In-plane elasticity of a novel auxetic honeycomb design," *Composites Part B: Engineering*, vol. 110, pp. 72–82, 2017.

[62] L. L. Hu, M. Z. Zhou, and H. Deng, "Dynamic crushing response of auxetic honeycombs under large deformation: Theoretical analysis and numerical simulation," *Thin-Walled Structures*, vol. 131, no. July, pp. 373–384, 2018.

[63] S. Shan, S. H. Kang, J. R. Raney, P. Wang, L. Fang, F. Candido, J. A. Lewis, and K. Bertoldi, "Multistable Architected Materials for Trapping Elastic Strain Energy," *Advanced Materials*, vol. 27, no. 29, pp. 4296–4301, 2015.

[64] T. R. Giri and R. Mailen, "Controlled snapping sequence and energy absorption in multistable mechanical metamaterial cylinders," *International Journal of Mechanical Sciences*, vol. 204, no. April, p. 106541, 2021.

[65] H. Yang and L. Ma, "1D to 3D multi-stable architected materials with zero Poisson's ratio and controllable thermal expansion," *Materials and Design*, vol. 188, pp. 1–16, 2020.

[66] G. N. Greaves, A. Greer, R. S. Lakes, and T. Rouxel, "Poisson's ratio and modern materials," *Nature materials*, vol. 10, no. 11, pp. 823–837, 2011.

[67] D. Li, L. Dong, and R. S. Lakes, "The properties of copper foams with negative poisson's ratio via resonant ultrasound spectroscopy," *physica status solidi (b)*, vol. 250, no. 10, pp. 1983–1987, 2013.

[68] R. Lakes and K. Elms, "Indentability of conventional and negative poisson's ratio foams," *Journal of Composite Materials*, vol. 27, no. 12, pp. 1193–1202, 1993.

[69] J. Choi and R. Lakes, "Fracture toughness of re-entrant foam materials with a negative poisson's ratio: experiment and analysis," *International Journal of fracture*, vol. 80, no. 1, pp. 73–83, 1996.

[70] S. Babaee, J. Shim, J. C. Weaver, E. R. Chen, N. Patel, and K. Bertoldi, "3d soft metamaterials with negative poisson's ratio," *Advanced Materials*, vol. 25, no. 36, pp. 5044–5049, 2013.

[71] H. Zhang, X. Guo, J. Wu, D. Fang, and Y. Zhang, "Soft mechanical metamaterials with unusual swelling behavior and tunable stress-strain curves," *Science advances*, vol. 4, no. 6, p. eaar8535, 2018.

[72] X. Ren, R. Das, P. Tran, T. D. Ngo, and Y. M. Xie, "Auxetic metamaterials and structures: a review," *Smart materials and structures*, vol. 27, no. 2, p. 023001, 2018.

[73] B. Howell, P. Prendergast, and L. Hansen, "Examination of acoustic behavior of negative poisson's ratio materials," *Applied Acoustics*, vol. 43, no. 2, pp. 141–148, 1994.

[74] H. N. Wadley, "Multifunctional periodic cellular metals," *Philosophical Transactions of the Royal Society A: Mathematical, Physical and Engineering Sciences*, vol. 364, no. 1838, pp. 31–68, 2006.

[75] J. Zhang, G. Lu, Z. Wang, D. Ruan, A. Alomarah, and Y. Durandet, "Large deformation of an auxetic structure in tension: experiments and finite element analysis," *Composite Structures*, vol. 184, pp. 92–101, 2018.

[76] J. Zhang, G. Lu, D. Ruan, and Z. Wang, "Tensile behavior of an auxetic structure: Analytical modeling and finite element analysis," *International Journal of Mechanical Sciences*, vol. 136, pp. 143–154, 2018.

[77] A. Alomarah, D. Ruan, and S. Masood, "Tensile properties of an auxetic structure with re-entrant and chiral features—a finite element study," *The International Journal of Advanced Manufacturing Technology*, vol. 99, no. 9-12, pp. 2425–2440, 2018.

[78] M. Fu, O. Xu, L. Hu, and T. Yu, "Nonlinear shear modulus of re-entrant hexagonal honeycombs under large deformation," *International Journal of Solids and Structures*, vol. 80, pp. 284–296, 2016.

[79] Z. Dong, Y. Li, T. Zhao, W. Wu, D. Xiao, and J. Liang, "Experimental and numerical studies on the compressive mechanical properties of the metallic auxetic reentrant honeycomb," *Materials & Design*, vol. 182, p. 108036, 2019.

[80] M. Lei, W. Hong, Z. Zhao, C. Hamel, M. Chen, H. Lu, and H. J. Qi, "3d printing of auxetic metamaterials with digitally reprogrammable shape," *ACS applied materials & interfaces*, vol. 11, no. 25, pp. 22768–22776, 2019.

[81] X. Ren, J. Shen, P. Tran, T. D. Ngo, and Y. M. Xie, "Design and characterisation of a tuneable 3d buckling-induced auxetic metamaterial," *Materials & Design*, vol. 139, pp. 336–342, 2018.

[82] K. Wang, Y.-H. Chang, Y. Chen, C. Zhang, and B. Wang, "Designable dual-material auxetic metamaterials using three-dimensional printing," *Materials & Design*, vol. 67, pp. 159–164, 2015.

[83] C. Ma, H. Lei, J. Liang, W. Wu, T. Wang, and D. Fang, "Macroscopic mechanical response of chiral-type cylindrical metastructures under axial compression loading," *Materials & Design*, vol. 158, pp. 198–212, 2018.

[84] Y. Yap and W. Yeong, "Shape recovery effect of 3d printed polymeric honeycomb: This paper studies the elastic behaviour of different honeycomb structures produced by polyjet technology," *Virtual and Physical Prototyping*, vol. 10, no. 2, pp. 91–99, 2015.

[85] A. Rafsanjani and D. Pasini, "Bistable auxetic mechanical metamaterials inspired by ancient geometric motifs," *Extreme Mechanics Letters*, vol. 9, pp. 291–296, 2016.

[86] F. Habib, P. Iovenitti, S. Masood, and M. Nikzad, "In-plane energy absorption evaluation of 3d printed polymeric honeycombs," *Virtual and Physical Prototyping*, vol. 12, no. 2, pp. 117–131, 2017.

[87] R. Hedayati, M. Sadighi, M. Mohammadi Aghdam, and A. A. Zadpoor, "Mechanical properties of additively manufactured thick honeycombs," *Materials*, vol. 9, no. 8, p. 613, 2016.

[88] R. Hedayati, M. Sadighi, M. Mohammadi-Aghdam, and A. Zadpoor, "Mechanical properties of additively manufactured octagonal honeycombs," *Materials Science and Engineering: C*, vol. 69, pp. 1307–1317, 2016.

[89] S. R. Bates, I. R. Farrow, and R. S. Trask, "3d printed elastic honeycombs with graded density for tailorable energy absorption," in *Active and Passive Smart Structures and*

Integrated Systems 2016, vol. 9799, p. 979907, International Society for Optics and Photonics, 2016.

[90] K. Van de Velde and P. Kiekens, "Biopolymers: overview of several properties and consequences on their applications," *Polymer testing*, vol. 21, no. 4, pp. 433–442, 2002.

[91] H. Yang and L. Ma, "Multi-stable mechanical metamaterials by elastic buckling instability," *Journal of Materials Science*, vol. 54, no. 4, pp. 3509–3526, 2019.

[92] Q. Chen, X. Zhang, and B. Zhu, "Design of buckling-induced mechanical metamaterials for energy absorption using topology optimization," *Structural and Multidisciplinary Optimization*, vol. 58, no. 4, pp. 1395–1410, 2018.

[93] S. Wasti and S. Adhikari, "Use of Biomaterials for 3D Printing by Fused Deposition Modeling Technique: A Review," *Frontiers in Chemistry*, vol. 8, no. May, pp. 1–14, 2020.

[94] S. Adanur and A. Jayswal, "Additive manufacturing of interlaced fibrous structures," *Rapid Prototyping Journal*, no. October 2020, 2021.

[95] J. Hua, H. Lei, Z. Zhang, C. Gao, and D. Fang, "Multistable Cylindrical Mechanical Metastructures: Theoretical and Experimental Studies," *Journal of Applied Mechanics, Transactions ASME*, vol. 86, no. 7, pp. 1–10, 2019.

[96] H. Yang and L. Ma, "1D and 2D snapping mechanical metamaterials with cylindrical topology," *International Journal of Solids and Structures*, vol. 204-205, pp. 220–232, 2020.

[97] Y. Guo, J. Zhang, L. Chen, B. Du, H. Liu, L. Chen, W. Li, and Y. Liu, "Deformation behaviors and energy absorption of auxetic lattice cylindrical structures under axial crushing load," *Aerospace Science and Technology*, vol. 98, p. 105662, 2020.

[98] B. Wang, X. Tan, S. Zhu, S. Chen, K. Yao, P. Xu, L. Wang, H. Wu, and Y. Sun, "Cushion performance of cylindrical negative stiffness structures: Analysis and optimization," *Composite Structures*, vol. 227, no. July, 2019.

[99] B. Chen, L. Chen, B. Du, H. Liu, W. Li, and D. Fang, "Novel multifunctional negative stiffness mechanical metamaterial structure: Tailored functions of multi-stable and compressive mono-stable," *Composites Part B: Engineering*, vol. 204, no. October 2020, p. 108501, 2021.

[100] M. Corsi, S. Bagassi, M. C. Moruzzi, and F. Weigand, "Additively manufactured negative stiffness structures for shock absorber applications," *Mechanics of Advanced Materials and Structures*, vol. 0, no. 0, pp. 1–12, 2020.

[101] S. Xu, Z. Yan, K. I. Jang, W. Huang, H. Fu, J. Kim, Z. Wei, M. Flavin, J. McCracken, R. Wang, A. Badea, Y. Liu, D. Xiao, G. Zhou, J. Lee, H. U. Chung, H. Cheng, W. Ren, A. Banks, X. Li, U. Paik, R. G. Nuzzo, Y. Huang, Y. Zhang, and J. A. Rogers, "Assembly of micro/nanomaterials into complex, three-dimensional architectures by compressive buckling," *Science*, vol. 347, no. 6218, pp. 154–159, 2015.

[102] A. Rafsanjani, A. Akbarzadeh, and D. Pasini, "Snapping Mechanical Metamaterials under Tension," *Advanced Materials*, vol. 27, no. 39, pp. 5931–5935, 2015.

[103] J. Liu, H. Qin, and Y. Liu, "Dynamic behaviors of phase transforming cellular structures," *Composite Structures*, vol. 184, no. April 2017, pp. 536–544, 2018.

[104] H. Yang and L. Ma, "Angle-Dependent Transitions Between Structural Bistability and Multistability," *Advanced Engineering Materials*, vol. 22, no. 5, pp. 1–10, 2020.

[105] C. Findeisen, J. Hohe, M. Kadic, and P. Gumbsch, "Characteristics of mechanical metamaterials based on buckling elements," *Journal of the Mechanics and Physics of Solids*, vol. 102, pp. 151–164, 2017.

[106] K. Che, C. Yuan, H. J. Qi, and J. Meaud, "Viscoelastic multistable architected materials with temperature-dependent snapping sequence," *Soft Matter*, vol. 14, no. 13, pp. 2492–2499, 2018.

[107] C. Valencia, D. Restrepo, N. D. Mankame, P. D. Zavattieri, and J. Gomez, "Computational characterization of the wave propagation behavior of multi-stable periodic cellular materials," *Extreme Mechanics Letters*, vol. 33, p. 100565, 2019.

[108] K. Che, C. Yuan, J. Wu, H. J. Qi, and J. Meaud, "Three-dimensional-printed multistable mechanical metamaterials with a deterministic deformation sequence," *Journal of Applied Mechanics, Transactions ASME*, vol. 84, no. 1, pp. 1–10, 2017.

[109] X. Tan, S. Chen, B. Wang, S. Zhu, L. Wu, and Y. Sun, "Design, fabrication, and characterization of multistable mechanical metamaterials for trapping energy," *Extreme Mechanics Letters*, vol. 28, pp. 8–21, 2019.

[110] Y. Zhang, M. Tichem, and F. van Keulen, "Rotational snap-through behavior of multi-stable beam-type metastructures," *International Journal of Mechanical Sciences*, vol. 193, no. June 2020, p. 106172, 2021.

[111] M. E. Pontecorvo, S. Barbarino, G. J. Murray, and F. S. Gandhi, "Bistable arches for morphing applications," *Journal of Intelligent Material Systems and Structures*, vol. 24, no. 3, pp. 274–286, 2013.

[112] J. Meaud and K. Che, "Tuning elastic wave propagation in multistable architected materials," *International Journal of Solids and Structures*, vol. 122-123, pp. 69–80, 2017.

[113] S. Sun, N. An, G. Wang, M. Li, and J. Zhou, "Achieving selective snapping-back and enhanced hysteresis in soft mechanical metamaterials via fiber reinforcement," *Journal of Applied Physics*, vol. 129, no. 4, 2021.

[114] K. Bertoldi, "Harnessing Instabilities to Design Tunable Architected Cellular Materials," *Annual Review of Materials Research*, vol. 47, pp. 51–61, 2017.

[115] J. Shim, P. Wang, and K. Bertoldi, "Harnessing instability-induced pattern transformation to design tunable phononic crystals," *International Journal of Solids and Structures*, vol. 58, pp. 52–61, 2015.

[116] X. Tan, B. Wang, Y. Yao, K. Yao, Y. Kang, S. Zhu, S. Chen, and P. Xu, "Programmable Buckling-based negative stiffness metamaterial," *Materials Letters*, vol. 262, p. 127072, 2020.

[117] B. M. Goldsberry and M. R. Haberman, "Negative stiffness honeycombs as tunable elastic metamaterials," *Journal of Applied Physics*, vol. 123, no. 9, 2018.

[118] K. R. Olympio and F. Gandhi, "Flexible skins for morphing aircraft using cellular honeycomb cores," *Journal of Intelligent Material Systems and Structures*, vol. 21, no. 17, pp. 1719–1735, 2010.

[119] R. M. Neville, F. Scarpa, and A. Pirrera, "Shape morphing Kirigami mechanical metamaterials," *Scientific Reports*, vol. 6, no. August, pp. 1–12, 2016.

[120] A. Rafsanjani and D. Pasini, "Bistable auxetic mechanical metamaterials inspired by ancient geometric motifs," *Extreme Mechanics Letters*, vol. 9, pp. 291–296, 2016.

[121] B. Haghpanah, L. Salari-Sharif, P. Pourrajab, J. Hopkins, and L. Valdevit, "Multistable Shape-Reconfigurable Architected Materials," *Advanced Materials*, vol. 28, no. 36, pp. 7915–7920, 2016.

[122] T. A. Hewage, K. L. Alderson, A. Alderson, and F. Scarpa, "Double-Negative Mechanical Metamaterials Displaying Simultaneous Negative Stiffness and Negative Poisson's Ratio Properties," *Advanced Materials*, vol. 28, no. 46, pp. 10323–10332, 2016.

[123] A. Zareei, B. Deng, and K. Bertoldi, "Harnessing transition waves to realize deployable structures," *Proceedings of the National Academy of Sciences of the United States of America*, vol. 117, no. 8, pp. 4015–4020, 2020.

[124] J. Sun, Q. Guan, Y. Liu, and J. Leng, "Morphing aircraft based on smart materials and structures: A state-of-the-art review," *Journal of Intelligent Material Systems and Structures*, vol. 27, no. 17, pp. 2289–2312, 2016.

[125] A. Erol and J. Baur, "Analysis of multi-stable architectures for morphing structures," *ASME 2020 Conference on Smart Materials, Adaptive Structures and Intelligent Systems, SMASIS 2020*, 2020.

[126] P. Materials, E. I. Materials, P. Matrix, C. Materials, and P. Specimens, "Standard Test Method for Tensile Properties of Plastics 1," no. January 2004, pp. 1–15, 2006.

[127] L. Liu, P. Kamm, F. García-Moreno, J. Banhart, and D. Pasini, "Elastic and failure response of imperfect three-dimensional metallic lattices: the role of geometric defects induced by Selective Laser Melting," *Journal of the Mechanics and Physics of Solids*, vol. 107, pp. 160–184, 2017.

[128] M. Vangbo, "An analytical analysis of a compressed bistable buckled beam," *Sensors and Actuators, A: Physical*, vol. 69, no. 3, pp. 212–216, 1998.